

A novel protection strategy for microgrid based on estimated differential energy of fault currents

Ankan Chandra^{*}, G.K. Singh, Vinay Pant

Department of Electrical Engineering, Indian Institute of Technology Roorkee, Roorkee, Uttarakhand, 247667, India

ARTICLE INFO

Keywords:

Distributed generation
Microgrid protection
Teager-Kaiser energy operator
Energy difference signal
High impedance fault
Fault inception angle

ABSTRACT

The significant benefits of distributed generation (DG) integration in the emerging microgrid are compromised due to substantial challenges associated with the protection. Due to DG penetration, fault current becomes dynamic, leading to make conventional protection methods vulnerable. In order to address this serious issue, a simple and fast protection algorithm, based on Teager-Kaiser Energy Operator (TKEO) is proposed in this paper. This scheme extracts the energy of current signal, retrieved from both ends of the line using TKEO. For fault detection, energy difference of the current signals is used. In order to validate the effectiveness of this proposed scheme, 33 bus test microgrid system operating in both grid-connected and autonomous mode is presented. For evaluating the performance of proposed scheme, high impedance fault cases are also examined. The distinctiveness of the proposed algorithm is that it is principally relying on the energy difference of current signals, therefore it can subdue the difficulties associated with dynamic fault current. Moreover, it does not suffer from computational complexity; thus, inherently hastening the detection process. The test system is designed and simulated in PSCAD-EMTDC software, while MATLAB programming interface is used for developing and testing the proposed algorithm.

1. Introduction

1.1. Motivation and incitement

The continuous rise in power consumption has empowered the incorporation of distributed generation (DG) into the distribution system (DS), resulting in the evolution of active DS and microgrid. The proliferation of DG elevates the power generation and acts as auxiliary source of real and reactive power to assist primary generation for the power system [1]. Distributed energy resources (DERs) in microgrid facilitates high power quality and accomplishes the power system with reduced power disruptions and enhanced grid resiliency [2]. Regardless of these thriving benefits, DG penetration into the microgrid initiates substantial technical challenges in terms of protection and control [3–5]. Different locations of DGs make the fault current bidirectional. Moreover, DG penetration level, type of DG (Inverter Interfaced DG (IIDG), Rotating Machine based DG (RMDG)), and reconfiguration of the microgrid, i.e. shifting from Grid-Connected Mode Operation (GCMO) to Autonomous Mode Operation (AMO), and vice versa are essentially responsible for dynamic fault current [6]. This dynamic fault level

subdues the viability of conventional overcurrent relay (OCR) and imposes elusive challenge for protection [7, 8]. Effectively, the OCRs suffer from blinding in protection, false tripping and relay coordination issues [3, 5].

1.2. Literature review

In order to address the aforementioned technical issues, the concept of adaptive overcurrent protection (AOCP) has been introduced, which allows the OCRs to change their threshold dynamically according to the system state. In [9], an AOCP is presented based on local information of current, where the relay trip characteristics are updated by detecting the operational condition and DG outages. This scheme has considered the radial microgrid system and only three phase symmetrical fault is studied using positive sequence current. In [10], the positive and negative sequence superimposed current is used to implement the AOCP. In addition, by using the idea of phase change between pre-fault and post-fault superimposed sequence currents, the fault direction is obtained which helps in to mitigate the bidirectionality problem. To improve the feasibility of protection, a communication assisted dual-setting AOCP scheme is proposed in [11]. The main objective of

^{*} Corresponding author.

E-mail address: chandraankan05@gmail.com (A. Chandra).

<https://doi.org/10.1016/j.epsr.2022.108824>

Received 17 July 2022; Received in revised form 5 September 2022; Accepted 17 September 2022

Available online 26 September 2022

0378-7796/© 2022 Elsevier B.V. All rights reserved.

Nomenclature*Abbreviations*

AMLM	Autonomous Mode Looped Microgrid
AMO	Autonomous Mode Operation
AOC	Adaptive Overcurrent Protection
AMRM	Autonomous Mode Radial Microgrid
CWT	Continuous Wavelet Transform
DER	Distribution Energy Resource
DFIG	Doubly Fed Induction Generator
DG	Distributed Generation
DS	Distribution System
DWT	Discrete Wavelet Transform
EDS	Energy Difference Signal
EMD	Empirical Mode Decomposition
FFT	Fast Fourier Transform
FIA	Fault Inception Angle
FIT	Fault Inception Time
GCMO	Grid-Connected Mode Operation
GCRM	Grid-Connected Radial Microgrid
GCLM	Grid-Connected Looped Microgrid
GPS	Global Positioning System
HIF	High Impedance Fault
IIDG	Inverter Interfaced DG
IED	Intelligent Electronic Device
LG	Line-Ground
LL	Line-Line
LLG	Line-Line-Ground
LLLG	Line-line-Line-Ground
LRF	Low Resistance Fault
MRA	Multiresolution Analysis
OCR	Overcurrent Relay
PCC	Point of Common Coupling
PMU	Phasor Measurement Unit
PV	Photovoltaic
RMDG	Rotating Machine based DG
TDS	Time Dial Setting
TKEO	Teager-Kaiser Energy Operator
TKE	Teager-Kaiser Energy
WFT	Windowed Fourier Transform
WT	Wavelet Transform
WAMPS	Wide Area Monitoring and Protection System
$T, T_1 - T_4$	Transformers
H	Inertia constant
R_a	Armature resistance
x_d	d-axis reactance
x'_d	d-axis transient reactance
x''_d	d-axis sub-transient reactance
x_q	q-axis reactance
x'_q	q-axis transient reactance
x''_q	q-axis sub-transient reactance
R_s	Stator resistance

r_a	Wound rotor resistance
X_l	Stator leakage reactance
x_l	Wound rotor leakage reactance
x_{l1}	Positive sequence leakage reactance
I_μ	Magnetizing current
R_0	Zero sequence resistance
R_1	Positive sequence resistance
X_0	Zero sequence inductance
X_1	Positive sequence inductance
C_0	Zero sequence capacitance
C_1	Positive sequence capacitance
R_m	Magnetizing resistance
X_m	Magnetizing inductance
w_i	Eddy current loss
w_c	Copper loss
$L_1 - L_{33}$	Loads
R_f	Fault resistances
$\zeta(t)$	Continuous time signal
ω	Fundamental frequency in rad/s
φ	Phase
a	Amplitude
$\dot{\zeta}(t)$	First order derivation of $\zeta(t)$
$\ddot{\zeta}(t)$	Second order derivation of $\zeta(t)$
$\Psi_{\zeta(t)}$	TKE of continuous signal $\zeta(t)$
$\zeta[n]$	Discrete time signal
$\Psi_{\zeta[n]}$	TKE of discrete signal $\zeta[n]$
Ω	Digital frequency in rad/ sample
f	Fundamental frequency (Hz)
f_s	Sampling frequency (Hz)
$I_{1(k)}$	Measured current at k^{th} bus end
$I_{2(k+1)}$	Measured current at $(k+1)^{th}$ bus end
$I_{3(k+2)}$	Measured current at the adjacent line of $(k+1)^{th}$ bus end
$I_{1(k)}[n]_{p \in A,B,C}$	n^{th} sample of three-phase current measured at k^{th} bus end
$I_{2(k+1)}[n]_{p \in A,B,C}$	n^{th} sample of three-phase current measured at $(k+1)^{th}$ bus end
$I_{3(k+2)}[n]_{p \in A,B,C}$	n^{th} sample of three-phase current measured at the adjacent line of $(k+1)^{th}$ bus end
$\Psi_{1(k)}[n]_{p \in A,B,C}$	TKE of $I_{1(k)}[n]_{p \in A,B,C}$
$\Psi_{2(k+1)}[n]_{p \in A,B,C}$	TKE of $I_{2(k+1)}[n]_{p \in A,B,C}$
$\Psi_{3(k+2)}[n]_{p \in A,B,C}$	TKE of $I_{3(k+2)}[n]_{p \in A,B,C}$
$\mathcal{E}_{p \in A,B,C}$	Energy difference
$\Psi_{1(k)}^0$	TKE of zero sequence current measured at k^{th} bus end
$\Psi_{2(k+1)}^0$	TKE of zero sequence current measured at $(k+1)^{th}$ bus end
$\Psi_{1(k)}^A, \Psi_{1(k)}^B, \Psi_{1(k)}^C$	TKE of phase-A,B,C current measured at k^{th} bus end, respectively.
$\Psi_{2(k+1)}^A, \Psi_{2(k+1)}^B, \Psi_{2(k+1)}^C$	TKE of phase-A,B,C current measured at $(k+1)^{th}$ bus end, respectively.

this proposed scheme is to minimize the relay operating time, which is done by formulating non-linear optimization problem to determine the relay settings optimally. Furthermore, aiming to obtain optimal time dial setting (TDS) for the OCR, various approaches have used nonlinear programming tools that are solved by metaheuristic techniques [12, 13]. However, while performing these algorithms, the primary concern arises with the computational complexity and computation time. Moreover, selection of initial solution, premature convergence, and requirement of high storage, while executing the algorithm, are the other constrains for

these techniques. Modern digital relays (Intelligent Electronic Device (IED)) include automated relay adjustment settings, which provides the benefit of quick data acquisition. With the assessment of secure and high speed communication systems, the idea of centralized protection [14, 15] and multi-agent systems based protection have been established [16]. With the advancement in technology, wide area monitoring and protection system (WAMPS), assisted by phasor measurement unit (PMU) is established [17]. WAMPS is capable to obtain the information of system state and electrical parameters by PMU, which is enabled with

global positioning system (GPS) facility [18, 19]. These approaches, however are expensive and require expedite maintenance to assure proper synchronization and fast data acquisition between several IEDs and controllers of the substations. The artificial intelligence and machine learning has further augmented the protection paradigm, where support vector machine, long short-term memory, decision tree, data mining based approaches are predominantly implemented to establish the fault detection and classification algorithms [20–23].

Furthermore, signal processing-based techniques have been profoundly incorporated for microgrid fault detection, which evaluates frequency information collected from transient components of the signal. The windowed Fourier transform (WFT), continuous and discrete wavelet transform based fault diagnosis approaches are developed [24, 25]. Specifically, multilayer analysis of a signal using discrete wavelet transform (DWT) and multiresolution analysis (MRA) is significantly applied in this field [26]. However, these techniques require extensive frequency domain analysis at different degrees of decomposition in order to get a finer scale representation of the signal, resulting in decisive complexity. To handle the non-linear and non-stationary signals, adaptive decomposition algorithms such as empirical mode decomposition (EMD) has been developed [27]. However, it is a recursive decomposition process, which decomposes the signals into sub-signals called intrinsic mode functions. Signal Energy contained within the signal, contains significant amount of information about the signal. In order to analyse the signal, signal's energy can be computed by a special operator called Teager-Kaiser Energy Operator (TKEO), which shows that the energy of a signal can be realized in terms of its instantaneous amplitude and frequency [28]. This class of operator is an efficient tool for analysing amplitude-modulated-frequency-modulated signals and images due to its simplicity and excellent time-resolution capability [29]. It was primarily used in nonlinear speech signals and audio signal processing [30]. Later on, it was applied in power system and machine applications, where it is used for fault detection in parallel transmission line, fault detection during power swing [31], for estimation of amplitudes, frequencies, and phase characteristics in power system signals [32], and also for machine bearing fault detection [33].

This paper has explicitly presented a protection algorithm based on energy measurement of the current signal using TKEO. It performs the fault detection of a 33 bus microgrid comprised of both RMDG and IIDG. In this work, the performance of the proposed technique is evaluated by studying the microgrid system for four possible operating conditions, such as grid-connected radial microgrid (GCRM), grid-connected looped microgrid (GCLM), autonomous mode radial microgrid (AMRM), autonomous mode looped microgrid (AMLML). A simple approach is presented here, which requires the fault current signals to be extracted from both ends of the line, and by calculating the Teager-Kaiser Energy (TKE) difference of fault current, fault is detected. HIF cases are also explored to demonstrate effectiveness of the suggested approach.

1.3. Novelty and contribution of this work

The following are the main contributions of this work that demonstrate its novelty for the microgrid protection:

- i The proposed algorithm is a simplified approach to detect the fault, as it requires only three consecutive sample data and three mathematical operations to calculate energy of the signal. It is a time domain approach; therefore, inherently hastening the detection process by avoiding extensive frequency domain analysis of the signals.
- ii This technique does not require to change the threshold value according to microgrid operation states, which eliminates multiple threshold estimation process, leading to facilitate it as a generalized solution for any microgrid structure.
- iii It is a two stage algorithm method, where the second stage is only activated, if fault is detected at first stage, else not executed. In

second stage, only the zero-sequence current energy is calculated and along with the data already acquired in first stage is sufficient to classify the fault.

- iv This approach can efficiently detect both low resistance fault (LRF) and high impedance fault (HIF). Also, it can distinguish the faults with other power system disturbances (load swing, DG outage).

1.3.1. Manuscript structure

Rest of the paper is organized as, the 33 bus test microgrid system and description of case studies is mentioned in Section 2. In Section 3, detail theory and relevant equations of TKEO is produced. Section 4 illustrates the proposed technique in detail. The critical analysis of the result is discussed in Section 5, and also contains the performance of proposed scheme. The discussion and comparison is mentioned in Section 6, and finally the important conclusion is drawn in Section 7.

2. System description

2.1. Structure of the tested microgrid system

To accomplish the suggested fault detection approach, a 33 bus microgrid system is modelled in PSCAD simulation software as shown in Fig. 1. The microgrid is connected to a 69 kV, 100 MVA, 60 Hz primary distribution grid. Through a 69/11 kV distribution transformer, voltage is stepped down to maintain operating voltage of the test microgrid at 11 kV. Four different DGs are incorporated to form the microgrid. The synchronous generator is driven by a small hydro turbine, where mechanical-hydraulic control type hydro governor model is used. The synchronous generator is a salient-pole machine rated as 0.75 MVA, having line voltage of 0.6 kV. An interfacing transformer, T_1 is used which steps up the voltage at 11 kV to maintain grid voltage level. The PV system is rated at 0.5 MW consists of MPPT control, DC/DC converter, and finally the DC-AC conversion stage is done by a PV inverter having output voltage magnitude of 460 V operating at 60 Hz. Further it is stepped up by transformer T_2 for microgrid interfacing. The wind turbine (here detailed wind farm model of type-3 in PSCAD is considered) is having a doubly-fed wound-rotor induction generator rated at 2.5 MW and operates at a line voltage of 0.69 kV with a frequency of 60 Hz. Here in doubly fed induction generator (DFIG), for grid side converter, reactive power and DC link voltage are controlled, whereas for rotor side converter, the active and reactive powers are controlled. An interfacing transformer T_3 is used for grid interconnection. A four stroke, 12-cylinder internal combustion engine coupled with the synchronous generator is used to model a 2 MW diesel generator (DG-4). It is connected to Bus-23 through a grid interfacing transformer T_4 . For transformers PSCAD non-ideal transformer models are used. For the distribution line, the buses are placed 5 km away from each other. 11 kV, frequency dependant phase model is used that are enabled with steady-state frequency of 60 Hz. Here, three conductor delta tower configuration is used with enabled ideal transposition. The protection system consists of digital relays with feeder breaker unit (shown together) and placed at both the ends of the lines and also for each loads and DG units. One point of common coupling (PCC) relay and main breaker unit is placed for the utility grid protection. The specifications and system data are given in Table 1.

2.2. Description of case studies in this work

For the test 33 bus microgrid system, four operation modes have been considered, in which the microgrid is enabled to be reconfigured by the four static switches (SW₁-SW₄), as shown in the Fig. 1. The close state of the switch is depicted as '1', and open state by '0' and different operating states are given in Table 2. Under four different operating conditions of the microgrid, different fault cases are studied, where fault at middle of the line and also close-in fault is considered. Different fault

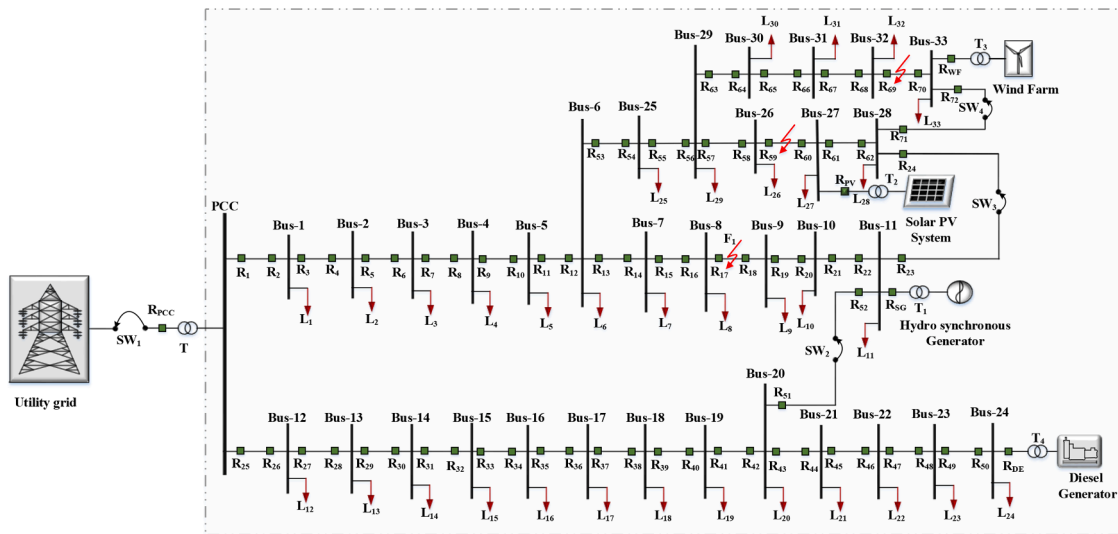


Fig. 1. 33 Bus test microgrid system.

Table 1
Rating and specifications of the modelled system.

- Distributed Generation (DG) units
- ✓ DG-1: Synchronous generator rated as 0.75 MVA connected at Bus-11 through transformer T₁.
 $H = 4 \text{ s}, f = 60 \text{ Hz}, R_a = 0.00517 \text{ pu}, x_d = 1.014 \text{ pu}, x'_d = 0.314 \text{ pu}, x''_d = 0.28 \text{ pu}, x_q = 0.77 \text{ pu}, x'_q = 0.328 \text{ pu}, x''_q = 0.288 \text{ pu}$
- ✓ DG-2: PV system rated at 0.5 MW connected at Bus-27 through interfacing transformer T₂.
 Number of modules connected in series/array= 40, number of module strings in parallel/array=8, number of cells connected in series/module=108, number of cell strings in parallel/module=4, reference irradiation=800–1200 W/m², reference cell temperature=25 °C-40 °C, series resistance/cell=0.02 Ω , shunt resistance/cell=1000 Ω . diode ideality factor=1.5.
- ✓ DG-3: DFIG based wind turbine rated at 2.5 MW connected at Bus-33 through an interfacing transformer T₃.
 $H = 3.2 \text{ s}, f = 60 \text{ Hz}, R_s = 0.0054 \text{ pu}, r_r = 0.00607 \text{ pu}, X_l = 0.1 \text{ pu}, \text{ and } x_l = 0.11 \text{ pu}$. Wind speed=7–15 m/s.
- ✓ DG-4: Diesel generator rated as 2 MW connected at Bus-24 through a grid interfacing transformer T₄.
 $H = 4.2 \text{ s}, f = 60 \text{ Hz}, R_a = 0.00725 \text{ pu}, x_d = 1.014 \text{ pu}, x'_d = 0.314 \text{ pu}, x''_d = 0.286 \text{ pu}, x_q = 0.771 \text{ pu}, x'_q = 0.328 \text{ pu}, x''_q = 0.288 \text{ pu}$.
- Transformers: PSCAD non-ideal transformer model.

Rating	R ₁ (pu)	X ₁ (pu)	R _m (pu)	X _m (pu)	x _{l1} (pu)	I _{μ} (%)	w ₁ (pu)	w _c (pu)
T 69/11 kV ($\Delta Yn1$), 100 MVA step-down transformer	0.00375	0.1	500	500	0.06	0.5	0.001	0.002
T ₁ 0.6/11 kV, ($\Delta Yn1$), 10 MVA step-up transformer.	0.00375	0.1	500	500	0.06	0.5	0.001	0.002
T ₂ 0.46/11 kV, ($\Delta Yn1$), 10MVA, step-up transformer.	0.00375	0.1	500	500	0.06	0.5	0.001	0.002
T ₃ 0.69/11 kV, ($\Delta Yn1$), 10 MVA step-up transformer.	0.00375	0.1	500	500	0.06	0.5	0.001	0.002
T ₄ 13.2/11 kV ($\Delta Yn1$), 10MVA step-down transformer.	0.00375	0.1	500	500	0.06	0.5	0.001	0.002

- Distribution line: PSCAD frequency dependant phase model, 11kV, 60 Hz.
 $R_0 = 0.0454 \Omega/\text{km}, R_1 = 0.0145 \Omega/\text{km}, X_0 = 1.37 \times 10^{-4} \text{H}/\text{km}, X_1 = 4.968 \times 10^{-5} \text{H}/\text{km}, C_0 = 4.981 \times 10^{-9} \text{F}/\text{km}, C_1 = 11.33 \times 10^{-9} \text{F}/\text{km}$;
 distance: 5 km each line segment.
- Load data: L₁ – L₃₃ each of 200 kW, 50 kVAR, rated load voltage=11.247 kV (rms).
 - Additional load data:
 - ✓ Load connection- disconnection event: 0.25 MW, 0.05 MVAR, rated load voltage=11.247 kV (rms).
 - ✓ Heavy loading event: Total of 25 MW, 5 MVAR, rated load voltage=11.247 kV (rms).

Table 2
Case study on the 33-Bus test microgrid system.

GCRM				GCLM				AMRM				AMLM			
SW ₁ =1, SW ₂ =0, SW ₃ =0, SW ₄ =0				SW ₁ =1, SW ₂ =1, SW ₃ =1, SW ₄ =1				SW ₁ =0, SW ₂ =0, SW ₃ =0, SW ₄ =0				SW ₁ =0, SW ₂ =1, SW ₃ =1, SW ₄ =1			
FIA=0° to 180°, in 15° interval				FIA=0° to 180°, in 15° interval				FIA=0° to 180°, in 15° interval				FIA=0° to 180°, in 15° interval			
R _f =0.01 Ω -100 Ω .				R _f =0.01 Ω -100 Ω .				R _f =0.01 Ω -100 Ω .				R _f =0.01 Ω -100 Ω .			
DG connected				DG connected/disconnected				DG connected				DG connected/disconnected			
Load connected/ disconnected				Load connected/ disconnected				Load connected/ disconnected				Load connected/ disconnected			
LG	LL	LLG	LLLG												
AG	AB	ABG	ABCG												
BG	BC	BCG		BG	BC	BCG		BG	BC	BCG		BG	BC	BCG	
CG	AC	ACG		CG	AC	ACG		CG	AC	ACG		CG	AC	ACG	
HIF				HIF				HIF				HIF			
LG		LLG	LLLG												
AG		ABG	ABCG												
BG		BCG		BG		BCG		BG		BCG		BG		BCG	
CG		ACG		CG		ACG		CG		ACG		CG		ACG	

resistances (R_f) are taken in the range between 0.01 Ω to 100 Ω , in order to cover low to high fault resistances. All the test cases are examined under varying fault inception angle (FIA), from 0° to 180° with an interval of 15°.

All ten type of fault cases, in which symmetrical LLLG (ABCG) and unsymmetrical fault LG (AG, BG, CG), LL (AB, BC, AB), LLG (ABG, BCG, ACG) faults with varying FIA and fault resistances are studied extensively at various positions of the microgrid as shown in Table 1. Nonetheless, to study the stochastic behaviour of HIF, a HIF model is developed, and comprehensively studied by simulating at different locations of the microgrid. Moreover, load and DG connection and disconnection cases, close-in fault detection, fault detection under heavy loading is also considered. Total of 1536 fault cases, for fault resistance varying between 10 and 100 Ω and fault inception angle 0°–180° is studied. For HIF, approximately 800 cases are studied with varying fault resistance and DC voltages of Emanuel's fault model. Likewise, for no fault, load switching, DG outage, DG intermittency, close-in fault, overloading cases, and no fault cases includes total 6476 case studies approximately.

3. Theoretical background of TKEO

Taking average of the sum of square of the magnitude of the signal is a common approach to compute the energy of a signal in time domain. In another manner, the energy of a signal can be found by the spectral energy obtained by Fourier transform that is the square of the signal's frequency spectrum, however it is acquired in frequency domain. The energy required to create a mono-component sinusoidal signal is also the product of fundamental frequency squared and the amplitude squared. For the sake of explanation, considering the continuous time signal $\zeta(t)$, presented in (1) having fundamental frequency ω , phase φ , and amplitude α . By the definition, the amount of energy required to generate the signal is $(\alpha^2 \cdot \omega^2)$. Hence, From Teager's initial idea, J. F. Kaiser has presented a simple technique to quantify the energy contained in a signal, based on its amplitude and frequency of oscillation. This energy measure of a signal is referred to as TKEO, and the obtained energy can be addressed as TKE [28]. This approach reaches up to the result of a signal's energy mentioned above as $(\alpha^2 \cdot \omega^2)$. To grasp this concept, first and second order derivatives are applied to continuous time signal $\zeta(t)$, and after performing trigonometric operations and rearrangements, identity obtained can be seen in (2), which relates the energy of a signal in terms of product of the square of fundamental frequency and square of its amplitude.

$$\zeta(t) = \alpha \cos(\omega t + \varphi) \quad (1)$$

$$\dot{\zeta}(t)^2 - \zeta(t) \cdot \ddot{\zeta}(t) = \alpha^2 \omega^2 \quad (2)$$

where, $\dot{\zeta}(t) = \frac{d\zeta(t)}{dt}$, and $\ddot{\zeta}(t) = \frac{d^2\zeta(t)}{dt^2}$, are the first and second order derivative of $\zeta(t)$ with respect to time respectively. Henceforth, it stands for the energy, and satisfies as an algorithm for obtaining signal's energy by simple mathematical operations. The continuous form of TKEO, applied to the continuous time signal $\zeta(t)$ is given in (3),

$$\Psi_{\zeta(t)} = \dot{\zeta}(t)^2 - \zeta(t) \cdot \ddot{\zeta}(t) \quad (3)$$

Further this technique implemented in case of discrete signal $\xi[n]$, shown in (4).

$$\xi[n] = \alpha \cos(\Omega n + \varphi) \quad (4)$$

where Ω is the digital frequency in radians/sample, n is the sample, and φ is the phase. Here,

$$\Omega = \frac{2\pi f}{f_s} \quad (5)$$

In which, f is the signal's analogue frequency, and f_s is the sampling

frequency. The two adjacent sample of (4), which are being taken into account in order to establish the mathematical identity can be seen form a set of equations as,

$$\left. \begin{aligned} \zeta[n-1] &= \alpha \cos(\Omega[n-1] + \varphi) \\ \zeta[n+1] &= \alpha \cos(\Omega[n+1] + \varphi) \end{aligned} \right\} \quad (6)$$

For computing the TKEO over a discrete time signal, three adjacent samples are required, and then after performing several mathematical operations, one would reach to the result depicted in (7).

$$\zeta[n+1] \cdot \zeta[n-1] = \zeta[n]^2 - \alpha^2 \sin^2(\Omega) \quad (7)$$

As it is known fact that for a small value of Ω , $\sin \Omega = \Omega$, so by limiting the value $\Omega < \frac{\pi}{4}$ that is taking the sampling frequency greater than eight times of the signal's frequency, the relative error can be minimized to 11%, and the energy operator gives the result established in (8), which is the energy contained in the signal [28].

$$\zeta[n]^2 - \zeta[n+1] \cdot \zeta[n-1] = \alpha^2 \Omega^2 \quad (8)$$

Therefore, TKEO can be established for the discrete signal as given in (9).

$$\Psi_{\zeta[n]} = \zeta[n]^2 - \zeta[n+1] \cdot \zeta[n-1] \quad (9)$$

Henceforth, it can be noticed that it is a simple and fast algorithm as it requires only two multiplications and one subtraction per point.

4. Proposed scheme for fault detection and fault type identification

In this proposed scheme, fault detection and classification have been done in two stages as shown in Fig. 2. In first stage, the algorithm essentially detects the fault and if fault is detected, it immediately sends trip signal to relays of the faulted line. Though the faulted line is recognized, this does not identify the fault type; therefore, the second stage is dedicated to classify the fault. From the illustration in Section 2, it can be seen that TKEO needs three adjacent equally spaced samples to perform the energy operation on a signal. To do so, current signals are first retrieved at both bus ends of the line. Here, for the generalization, k^{th} and $(k+1)^{\text{th}}$ bus have been considered, as shown in Fig. 2. First the current signals are retrieved at both ends of line, that is k^{th} and $(k+1)^{\text{th}}$ bus. Considering the current entering from k^{th} bus end towards the fault point F is $I_{1(k)p \in A,B,C}$, and the current entering from $(k+1)^{\text{th}}$ bus towards F is $I_{2(k+1)p \in A,B,C}$. The current signals are sampled with a frequency of 3.84 KHz, and three adjacent samples are collected. After which TKEO is performed to obtain the energy of the signal, given as (10) and (11).

$$\Psi_{1(k)p \in A,B,C} = I_{1(k)p}[n]^2 - I_{1(k)p}[n+1] \cdot I_{1(k)p}[n-1] \quad (10)$$

$$\Psi_{2(k+1)p \in A,B,C} = I_{2(k+1)p}[n]^2 - I_{2(k+1)p}[n+1] \cdot I_{2(k+1)p}[n-1] \quad (11)$$

The difference energy is obtained from the (11),

$$\mathcal{E}_{p \in A,B,C} = \Psi_{1(k)p \in A,B,C} - \Psi_{2(k+1)p \in A,B,C} \quad (12)$$

The fault detection criteria are set based on the analysis says, when $\mathcal{E}_{p \in A,B,C} > 0$; a fault has occurred in the line, and when $\mathcal{E}_{p \in A,B,C} = 0$, that is if the difference energy is zero, no fault has happened in the line for which the energy difference is calculated. This fault detection technique is based on the TKE difference of fault current signal. It is simple to understand the fact that under normal operating condition, current flowing through the same feeder is uni-directional at any particular instant, resulting in same TKE of the current signal, if measured at two ends of the line. As a result, TKE difference of the signal in such situation has to be zero, as it must be in all cases, where no disturbance occurs anywhere inside the line. If a disturbance occurs inside a line, then only the current converge to that point from both ends, except that the current flow in the line should remain uni-directional for a specific time, hence the threshold is set to zero in order to detect the fault. This

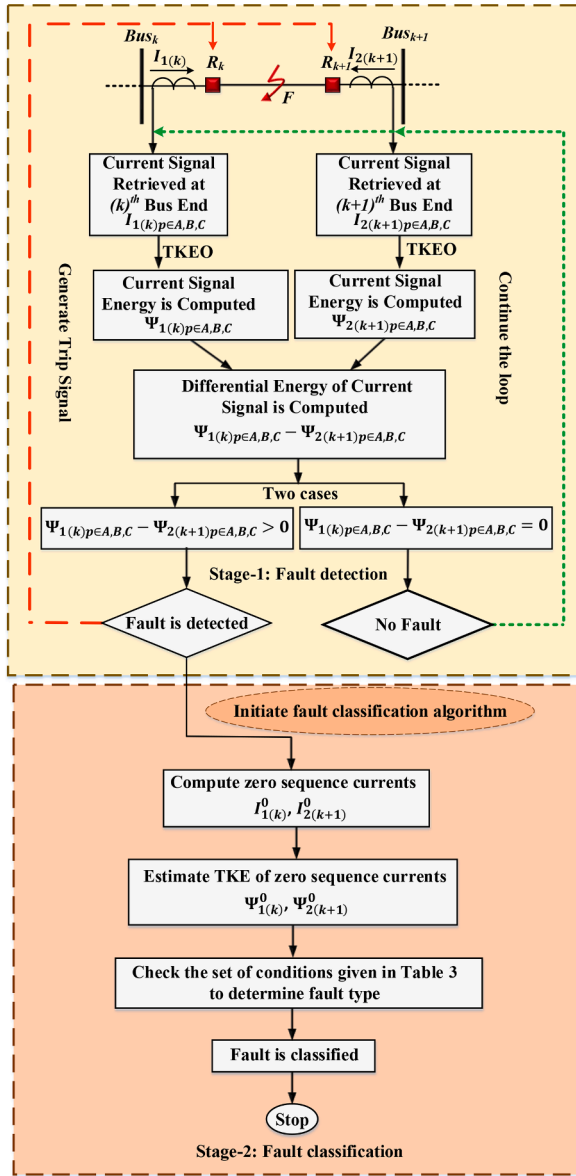


Fig. 2. Proposed fault detection and classification algorithm.

fundamental principle makes sense in this context. Fault incidence in that line may, therefore be validated by collecting the current signal from both ends of the line and determining the difference of TKE of the instantaneous current signal. To identify the fault, this idea has been applied to each line of the microgrid. The current magnitude and current flow direction may change due to the events such as unexpected load shifts, unplanned islanding, and disconnection of DG units. However, unless there is a disruption inside the line, the same current flows from one end to the other. This suggests that the current has the same TKE at both ends of the line, thus it won't misoperate for any of the aforementioned disruptions. As a result, this approach demonstrates its efficacy in the case of a fault scenario, when the current is reaching a spot from both ends. Only the Energy difference is detected at that moment, which confirms the fault condition.

As soon as the fault is detected, the trip signal is sent to both ends of the line in order to isolate the faulted section. In the second stage, the fault classification algorithm is initiated to identify the fault type, if from first stage, the fault is confirmed, as illustrated in Fig. 2. To execute the fault classification algorithm, zero-sequence current is obtained from the retrieved currents, using symmetrical component analysis. After

extracting zero sequence current, TKEO is applied to find energy of the zero sequence current. Since, zero sequence current is not present for unsymmetrical line-line fault and for balanced fault, it does not generate TKE of zero sequence current component. As a result, it serves as an excellent indicator to identify the fault type. The criterion has been given in Table 3. For unbalanced ground faults (LG and LLG), the fault current produces significant amount of zero sequence current, resulting in high TKE of the zero sequence current ($\Psi_{1(k)}^0$ & $\Psi_{2(k+1)}^0 \neq 0$). On the other hand, for non-grounded unbalanced fault (LL), the zero sequence current is absent (negligibly small in simulation study), therefore TKE of the zero sequence current for LL fault is ($\Psi_{1(k)}^0$ & $\Psi_{2(k+1)}^0 = 0$) zero or neglected. Same is true for balanced three phase fault (LLL or LLLG). Hence, this substantiate the fault classification.

5. Result analysis

5.1. Study of different fault scenario under different microgrid configurations

The established protection algorithm has been tested under different microgrid topologies as mentioned in Table 1. As this fault detection technique is based on the difference of current signal energy, the three phase current waveforms of both the sides are shown in the same frame, along with EDS and trip signal for all test cases.

5.1.1. Operation for GCRM

In order to perform GCRM configured operation, SW₁ is kept closed to retain microgrid connection with the utility grid, while SW₂, SW₃, and SW₄ are kept open (shown in Fig. 1). In Figs. 3–6, the symmetrical and unsymmetrical fault results have been shown, in which the fault resistance (R_f) is taken 0.01 Ω and FIA is considered to be 0°. Fault has occurred at middle of the line that is 2.5 km from the buses, connecting Bus-8 and Bus-9 (shown in Fig. 1). GCRM encompasses a current of 0.56 kA prior to the fault. The fault has occurred at 0.2 s, and energy difference signal (EDS) shows a sharp spike for LG(AG) fault, before which (in the interval 0 s to 0.2 s) the EDSs were zero for all three phases. After the occurrence of the fault, EDS for pH-A persists, whereas pH-B, pH-C retained zero. For LL(AB), LLG(ABG) and three-phase bolted symmetrical fault LLLG(ABCG), the fault current magnitude changes distinctly. Hence, the pattern associated with EDS is varying accordingly as TKE is

Table 3
Criteria for fault classification.

i.	When $\Psi_{1(k)}^A - \Psi_{2(k+1)}^A \neq 0$, $\Psi_{1(k)}^B - \Psi_{2(k+1)}^B = 0$, $\Psi_{1(k)}^C - \Psi_{2(k+1)}^C = 0$, and if $\Psi_{1(k)}^0$ & $\Psi_{2(k+1)}^0 \neq 0$	✓ AG (LG) fault.
ii.	When $\Psi_{1(k)}^A - \Psi_{2(k+1)}^A = 0$, $\Psi_{1(k)}^B - \Psi_{2(k+1)}^B \neq 0$, $\Psi_{1(k)}^C - \Psi_{2(k+1)}^C = 0$, and if $\Psi_{1(k)}^0$ & $\Psi_{2(k+1)}^0 \neq 0$	✓ BG (LG) fault.
iii.	When $\Psi_{1(k)}^A - \Psi_{2(k+1)}^A = 0$, $\Psi_{1(k)}^B - \Psi_{2(k+1)}^B = 0$, $\Psi_{1(k)}^C - \Psi_{2(k+1)}^C \neq 0$, and if $\Psi_{1(k)}^0$ & $\Psi_{2(k+1)}^0 \neq 0$	✓ CG (LG) fault.
iv.	When $\Psi_{1(k)}^A - \Psi_{2(k+1)}^A \neq 0$, $\Psi_{1(k)}^B - \Psi_{2(k+1)}^B \neq 0$, $\Psi_{1(k)}^C - \Psi_{2(k+1)}^C = 0$, and if $\Psi_{1(k)}^0$ & $\Psi_{2(k+1)}^0 = 0$	✓ AB (LL) fault.
v.	When $\Psi_{1(k)}^A - \Psi_{2(k+1)}^A = 0$, $\Psi_{1(k)}^B - \Psi_{2(k+1)}^B \neq 0$, $\Psi_{1(k)}^C - \Psi_{2(k+1)}^C \neq 0$, and if $\Psi_{1(k)}^0$ & $\Psi_{2(k+1)}^0 = 0$	✓ BC (LL) fault.
vi.	When $\Psi_{1(k)}^A - \Psi_{2(k+1)}^A \neq 0$, $\Psi_{1(k)}^B - \Psi_{2(k+1)}^B = 0$, $\Psi_{1(k)}^C - \Psi_{2(k+1)}^C \neq 0$, and if $\Psi_{1(k)}^0$ & $\Psi_{2(k+1)}^0 = 0$	✓ AC (LL) fault.
vii.	When $\Psi_{1(k)}^A - \Psi_{2(k+1)}^A \neq 0$, $\Psi_{1(k)}^B - \Psi_{2(k+1)}^B \neq 0$, $\Psi_{1(k)}^C - \Psi_{2(k+1)}^C = 0$, and if $\Psi_{1(k)}^0$ & $\Psi_{2(k+1)}^0 \neq 0$	✓ ABG (LLG) fault.
viii.	When $\Psi_{1(k)}^A - \Psi_{2(k+1)}^A = 0$, $\Psi_{1(k)}^B - \Psi_{2(k+1)}^B \neq 0$, $\Psi_{1(k)}^C - \Psi_{2(k+1)}^C \neq 0$, and if $\Psi_{1(k)}^0$ & $\Psi_{2(k+1)}^0 \neq 0$	✓ BCG (LLG) fault.
ix.	When $\Psi_{1(k)}^A - \Psi_{2(k+1)}^A \neq 0$, $\Psi_{1(k)}^B - \Psi_{2(k+1)}^B = 0$, $\Psi_{1(k)}^C - \Psi_{2(k+1)}^C \neq 0$, and if $\Psi_{1(k)}^0$ & $\Psi_{2(k+1)}^0 \neq 0$	✓ ACG (LLG) fault.
x.	When $\Psi_{1(k)}^A - \Psi_{2(k+1)}^A \neq 0$, $\Psi_{1(k)}^B - \Psi_{2(k+1)}^B \neq 0$, $\Psi_{1(k)}^C - \Psi_{2(k+1)}^C \neq 0$, and if $\Psi_{1(k)}^0$ & $\Psi_{2(k+1)}^0 = 0$	✓ ABCG (LLL) fault.

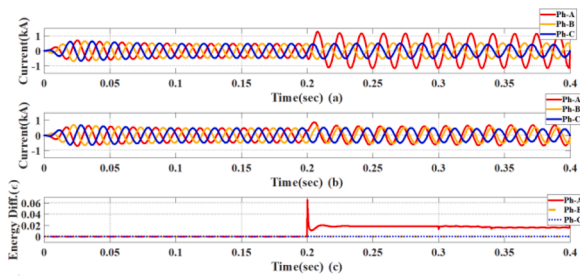


Fig. 3. LG (AG) Fault under GCRM, FIA=0°, $R_f=0.01 \Omega$, Fault at middle of the line (2.5 km from both buses) (a) Retrieved current signal at Bus-8 end, (b) Retrieved current signal at Bus-9 end, (c) EDS. .

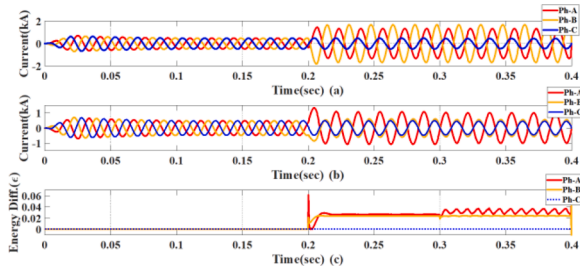


Fig. 4. LL (AB) Fault under GCRM, FIA=0°, $R_f=0.01 \Omega$, Fault at middle of the line (2.5 km from both buses) (a) Retrieved current signal at Bus-8 end, (b) Retrieved current signal at Bus-9 end, (c) EDS.

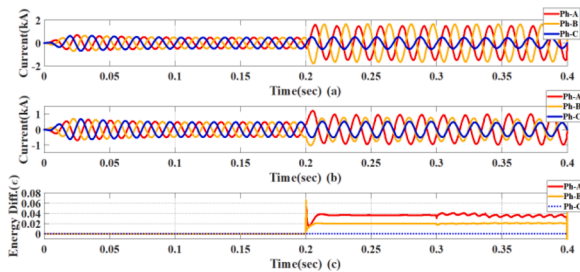


Fig. 5. LLG (ABG) Fault under GCRM, FIA=0°, $R_f=0.01 \Omega$, Fault at middle of the line (2.5 km from both buses) (a) Retrieved current signal at Bus-8 end, (b) Retrieved current signal at Bus-9 end, (c) EDS.

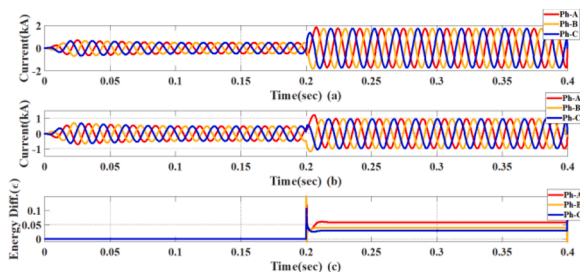


Fig. 6. LLLG (ABCG) Fault under GCRM, FIA=0°, $R_f=0.01 \Omega$, Fault at middle of the line (2.5 km from both buses) (a) Retrieved current signal at Bus-8 end, (b) Retrieved current signal at Bus-9 end, (c) EDS.

substantially depends on the product of signal's magnitude and square of the frequency. However, it is not affecting the detection process, which is examined, when high resistance fault ($R_f=100 \Omega$) is performed that poses very low fault current magnitude. From Figs. 3–6, it can be observed that EDS for the faulted phase sustained after the inception of fault, EDS for other phases retained zero throughout the duration of

fault. This primarily helps in to detect the faulted phase accurately with high selectivity.

5.1.2. Operation for GCLM

GCLM mode of operation is performed by closing all the switches (SW₁–SW₄), (can be seen from Fig. 1). In Figs. 7–10, all the fault results have been shown, in which the fault resistance (R_f) is taken 0.01Ω and FIA is considered to be 0° . The fault has occurred in the line connecting Bus-8 and Bus-9, at a distance 50% from Bus-8. In GCLM, the current level was 0.65 kA prior to fault; and during the fault, fault current reaches up to $1.2\text{--}1.8 \text{ kA}$ for different unsymmetrical and symmetrical faults. The fault has occurred at 0.2 s , and after detecting the fault, the generated trip signals have activated the relay R_{17} and R_{18} from both ends of the line to isolate the faulted line, so that the fault current can't propagate to healthy sections of the microgrid. The sharp spike at the instant 0.2 s and the non-zero value of EDS helps to detect the fault occurrence time and duration. Here to realize the characteristics of EDS, the fault duration is taken for longer period. This is also to verify the idea that EDS persist for the faulted phase(s) until the fault is extinguishing. Later it is again illustrated that how it helps facilitate to distinguish the fault accurately with high selectivity from other power system disturbances.

5.1.3. Operation for AMRM

AMRM poses low grid current around 0.4 kA due to disconnection with the utility grid. This mode of operation is commenced by opening all the switches (SW₁–SW₄). The result for symmetrical and unsymmetrical faults are shown in Figs. 11–14, considering the FIA to be 0° , with R_f being 0.01Ω . It is worth to be noted that the fault current magnitude ranges between 0.9 to 1 kA for all types of faults, leading to reduce the magnitude of EDS than that of GCLM mode. However, this detection process is instantaneous as one can see the initial peaks are occurred exactly at 0.2 s for all types of fault, and EDS sustained for the entire duration of fault. Before the occurrence of the fault, EDS was zero for all three phases; and after fault occurrence, energy difference fault indicating signal remain zero throughout the time other than the faulted phase (B-pH, C-pH for AG fault, C-pH for AB and ABG fault). This phenomenon is so spontaneous and happening irrespective of the difference of large magnitude of currents I_1 and I_2 . The fault current magnitude at a particular instant for 'A' phase of I_1 current and 'A' phase of I_2 current need not differ much in magnitude to establish the EDS. However, the difference signal is not maintained at a fixed magnitude as the difference of current magnitude of two fault currents, which are changing instantaneously.

5.1.4. Operation for AMLM

AMLM configuration has been executed by opening SW₁, which disconnects the microgrid from the utility, while SW₂–SW₄ remain closed to from the loop configuration. The operating current level prior to the fault is 0.48 kA , and it reaches to maximum 1.1 kA for three phase bolted symmetrical fault as shown in Fig. 18. The results for

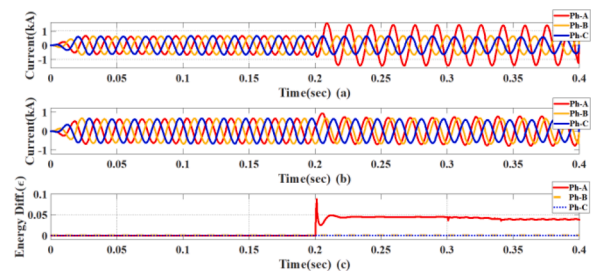


Fig. 7. LG (AG) Fault under GCLM, FIA=0°, $R_f=0.01 \Omega$, Fault at middle of the line (2.5 km from both buses) (a) Retrieved current signal at Bus-8 end, (b) Retrieved current signal at Bus-9 end, (c) EDS.

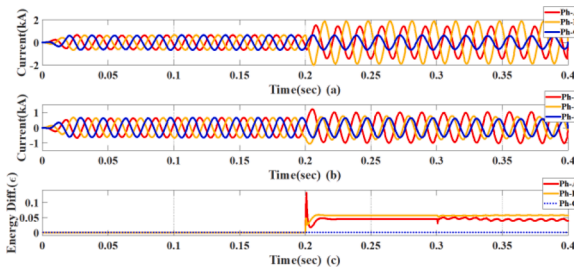


Fig. 8. LL (AB) Fault under GCLM, $FIA=0^\circ$, $R_f=0.01 \Omega$, Fault at middle of the line (2.5 km from both buses) (a) Retrieved current signal at Bus-8 end, (b) Retrieved current signal at Bus-9 end, (c) EDS.

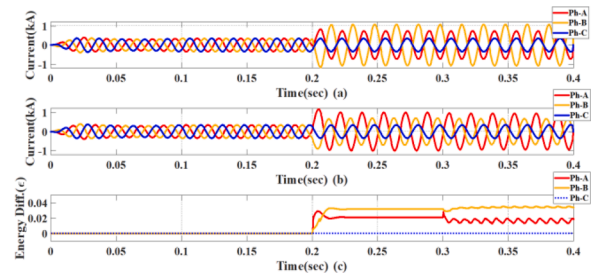


Fig. 12. LL (AB) Fault under AMRM, $FIA=0^\circ$, $R_f=0.01 \Omega$, Fault at middle of the line (2.5 km from both buses) (a) Retrieved current signal at Bus-8 end, (b) Retrieved current signal at Bus-9 end, (c) EDS.

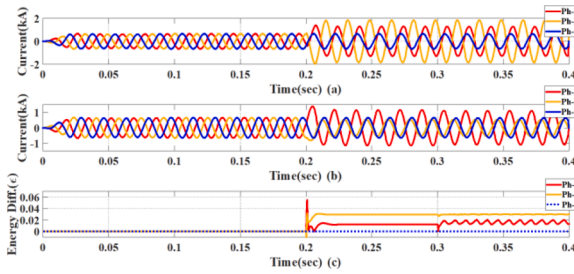


Fig. 9. LLG (ABG) Fault under GCLM, $FIA=0^\circ$, $R_f=0.01 \Omega$, Fault at middle of the line (2.5 km from both buses) (a) Retrieved current signal at Bus-8 end, (b) Retrieved current signal at Bus-9 end, (c) EDS.

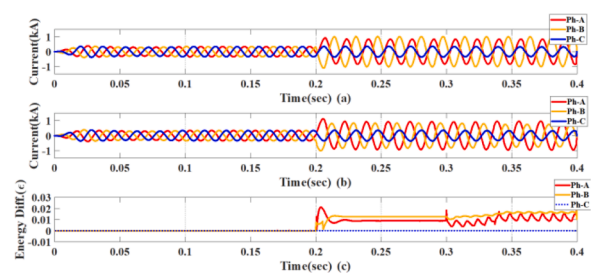


Fig. 13. LLG (ABG) Fault under AMRM, $FIA=0^\circ$, $R_f=0.01 \Omega$, Fault at middle of the line (2.5 km from both buses) (a) Retrieved current signal at Bus-8 end, (b) Retrieved current signal at Bus-9 end, (c) EDS.

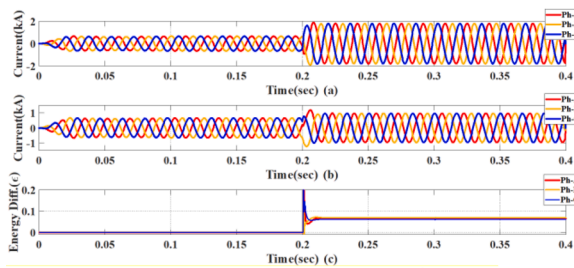


Fig. 10. LLLG (ABCG) Fault under GCLM, $FIA=0^\circ$, $R_f=0.01 \Omega$, Fault at middle of the line (2.5 km from both buses) (a) Retrieved current signal at Bus-8 end, (b) Retrieved current signal at Bus-9 end, (c) EDS.

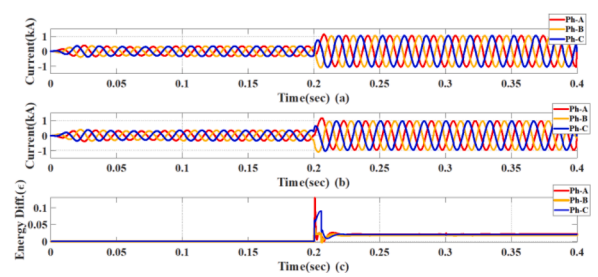


Fig. 14. LLLG (ABCG) Fault under AMRM, $FIA=0^\circ$, $R_f=0.01 \Omega$, Fault at middle of the line (2.5 km from both buses) (a) Retrieved current signal at Bus-8 end, (b) Retrieved current signal at Bus-9 end, (c) EDS.

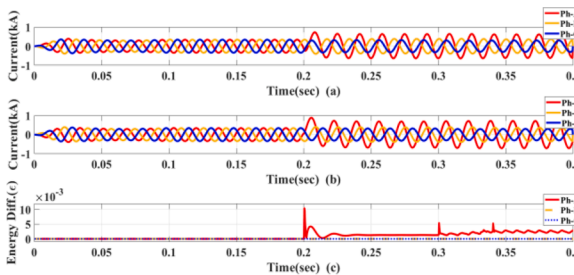


Fig. 11. LG (AG) Fault under AMRM, $FIA=0^\circ$, $R_f=0.01 \Omega$, Fault at middle of the line (2.5 km from both buses) (a) Retrieved current signal at Bus-8 end, (b) Retrieved current signal at Bus-9 end, (c) EDS.

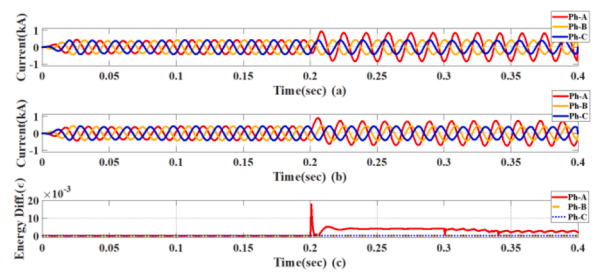


Fig. 15. LG (AG) Fault under AMLM, $FIA=0^\circ$, $R_f=0.01 \Omega$, Fault at middle of the line (2.5 km from both buses) (a) Retrieved current signal at Bus-8 end, (b) Retrieved current signal at Bus-9 end, (c) EDS.

unsymmetrical faults (AG, AB, ABG) are depicted in Figs. 15–17. Here also the FIA is set to be 0° and fault resistance is set to 0.01Ω . The effect of high fault resistance and varying FIA have been illustrated in next section. It is to be noted that the generated energy difference fault detection signals are showing uncertainties in pattern, which is due to the fact that the TKEO is a nonlinear process, and this energy operator is directly proportional to the square of the two time varying parameters

magnitude and frequency. Therefore, the oscillatory nature of signal attributed to uneven nature of EDS. The results provided in the next section are explicit as those shows how this EDS can change its pattern in dynamic and stochastic fault current for HIFs.

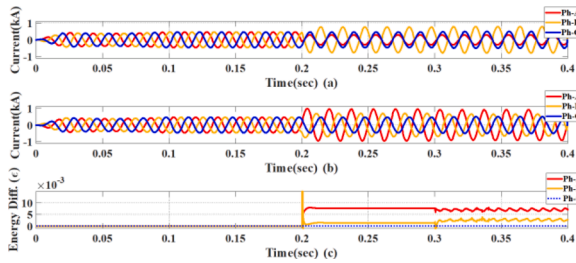


Fig. 16. LL (AB) Fault under AMLM, FIA=0°, R_f=0.01 Ω, Fault at middle of the line (2.5 km from both buses) (a) Retrieved current signal at Bus-8 end, (b) Retrieved current signal at Bus-9 end, (c) EDS.

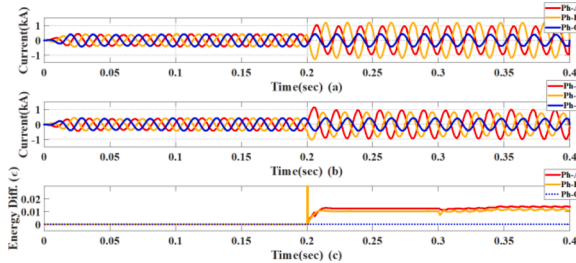


Fig. 17. LLG (ABG) Fault under AMLM, FIA=0°, R_f=0.01 Ω, Fault at middle of the line (2.5 km from both buses) (a) Retrieved current signal at Bus-8 end, (b) Retrieved current signal at Bus-9 end, (c) EDS.

5.2. Performance evaluation of the proposed scheme

5.2.1. Three phase symmetrical and unsymmetrical fault (Effect of fault resistances and FIA)

FIA is the angle of voltage phasor of the line right before the short circuit with ground. As this is 60 Hz system, therefore voltage wave completes 12 full cycles in 200 ms (0.2 s), i.e. at 200th ms, pH-A voltage passes through zero-crossing again. Hence, if the fault is to be incepted at 200 ms, the FIA for pH-A is 0°. The system is tested for all FIA, occurring at an interval of 15°, as shown in Table 4. fault inception time (FIT) determines the FIA, which can potentially affect the magnitude and nature of EDS. The instantaneous current produces instantaneous energy, thus the energy difference pattern changes accordingly. Here four different cases are studied under different FIA, with varying fault resistance (R_f) and different microgrid topologies, as shown in Figs. 19–22. LG(AG) fault has been examined under GCLM with FIA, 30° and R_f is taken 10Ω. Due to 30° FIA, the fault inception has been simulated at 0.20138s (given in Table 3), as shown in Fig. 19. While comparing it with Fig. 7, where the fault was studied with 0° FIA and R_f of 0.01 Ω, it can be noticed that the fault current magnitude has reduced due to increased fault resistance. The EDS magnitude is also reduced after the initial spike, however it was essentially retained for the entire duration of the fault.

Moreover, to evaluate the performance accuracy, LL(AB) fault under GCRM, with FIA of 45° and R_f of 50Ω simulated at 0.20208s (given in Table 4), and shown in Fig. 20 can be compared with Fig. 4. A LLG (ABG) fault under AMRM, with FIA of 60°, and R_f of 100Ω, simulated at 0.20277s (given in Table 4), and shown in Fig. 21 can be compared with

Table 4
FIT corresponding FIA.

FIT(ms)	200	200.69	201.38	202.08	202.77	203.47	204.16	204.86	205.55	206.25	206.94	207.63	208.33
FIA in degree													
pH-A	0°	15°	30°	45°	60°	75°	90°	105°	120°	135°	150°	165°	180°
pH-B	240°	255°	270°	285°	300°	315°	330°	345°	360°/0°	15°	30°	45°	60°
pH-C	120°	135°	150°	165°	180°	195°	210°	225°	240°	255°	270°	285°	300°

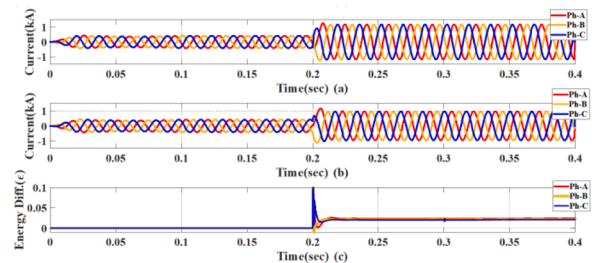


Fig. 18. LLLG (ABCG) Fault under AMLM, FIA=0°, R_f=0.01 Ω, Fault at middle of the line (2.5 km from both buses) (a) Retrieved current signal at Bus-8 end, (b) Retrieved current signal at Bus-9 end, (c) EDS.

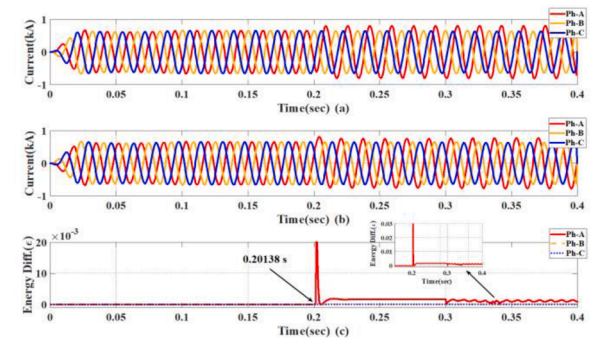


Fig. 19. LG (AG) Fault under GCLM, FIA=30°, R_f=10Ω Fault at middle of the line (2.5 km from both buses) (a) Retrieved current signal at Bus-8 end, (b) Retrieved current signal at Bus-9 end (c) EDS. .

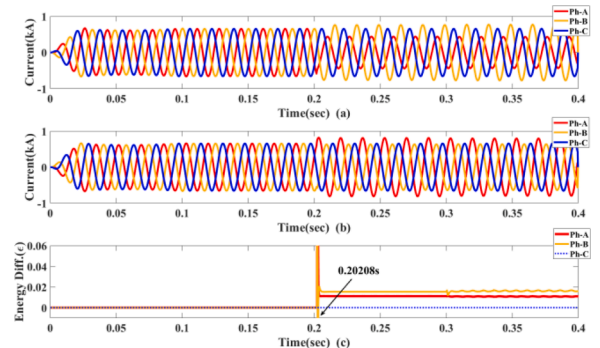


Fig. 20. LL (AB) Fault under GCRM, FIA=45°, R_f=50Ω, Fault at middle of the line (2.5 km from both buses) (a) Retrieved current signal at Bus-8 end, (b) Retrieved current signal at Bus-9 end, (c) EDS. .

Fig. 13. Nonetheless, as shown in Fig. 22, LLLG (ABCG) fault under AMLM, having FIA of 90°, with R_f of 50Ω, simulated at 0.20416 s (given in Table 4) and can be compared with Fig. 18. From the observation, it is evident that the fault is detected accordingly with varying FIA. Due to high fault resistance, the fault current magnitude has substantially reduced, which has an impact on the magnitude of EDS as TKE essentially varies with instantaneous magnitude, however it does not affect the generation of EDS. Moreover, FIA have not introduced any specific

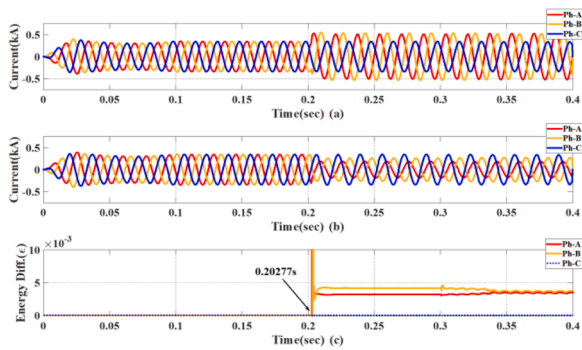


Fig. 21. LLG (ABG) Fault under AMRM, FIA=60°, R_f=100Ω, Fault at middle of the line (2.5 km from both buses) (a) Retrieved current signal at Bus-8 end, (b) Retrieved current signal at Bus-9 end, (c) EDS. .

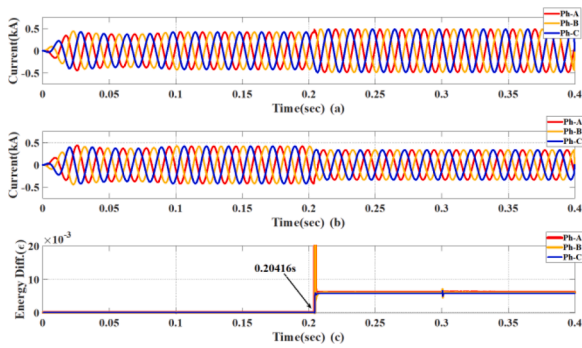


Fig. 22. LLLG (ABCG) Fault under AMLM, FIA=90°, R_f=50Ω, Fault at middle of the line (2.5 km from both buses) (a) Retrieved current signal at Bus-8 end, (b) Retrieved current signal at Bus-9 end, (c) EDS. .

hindrance for EDS, henceforth this technique can seamlessly operate under varying fault resistance, and FIA won't subdue its performance accuracy.

5.2.2. HIF detection

Detection of HIF is challenging due to its relatively low fault current magnitude near to full load rated current. Moreover, HIF current characteristics are nonlinearly deterministic or stochastic, and has a prolonged effect into the system [34]. As the waveform of HIF contains peculiar characteristics of build-up, shoulder, non-linearity, and asymmetry in the waveform, modelling of protection strategy that can work

accurately for both LRF as well as HIF is a difficult task. HIF in fact happens, when broken wire of the overhead power line falls on a poor conductive surface that encompasses very high resistance. In order to realize that the 'Emanuel HIF model' is developed so that similar impact of real fault in line can be ensured as this model has essentially considered the presence of an electric arc at the fault point [35]. As shown in Fig. 23(a), three separate unites are engaged with three phases. This model (a single unit) consists of two DC voltage sources (V₁, V₂) resembling arc voltage of air in the surface or between surface and power line. Two anti-parallel diodes in series with resistance (D₁-R₁ & D₂-R₂) resembles the non-linearity of earth or fault surface resistance. Here, the switches are used to connect or disconnect the HIF model unit, switches (S₁, S₂, S₃) with the power line, while (S_{AG}, S_{BG}, S_{CG}) are for ground and (S_{AB}, S_{BC}, S_{AC}) are for LLG-HIF simulation. Fig. 23(b) shows the obtained voltage-current characteristics curve of Emanuel model of HIF. The results are shown in Figs. 24–27, for different HIF cases under different microgrid configurations (GCRM & AMRM) in the line connecting Bus-30, 31 (can be seen from Fig. 1). Here, the fault current from Bus-31 for LG(CG) under GCRM shown in Fig. 24(b), is consisting of non-linearity, asymmetry, whereas HIF-LLG(BCG) fault current under AMRM is comprising arc and shoulders, can be seen in Fig. 25(a), (b). In case of HIF-LLG (ABCG), the fault current is visibly indistinguishable from full load current, given in Fig. 27. The fault initiates, when power line voltage exceeds the positive DC voltage (V₁) (here it is incepted at 0.2 s), but to inhibit the reverse current from negative DC voltage (V₂), V₂ must be greater than V₁. The operating parameters and switching operations are given in Tables 5 and 6 respectively. From the observation, it can be seen that HIF current contains different harmonics, which is the function of voltage deviation of the DC voltage sources of the Emanuel HIF test model. The EDSs, therefore exhibits distinct patterns for different HIFs due to the presence of harmonic frequency, varying

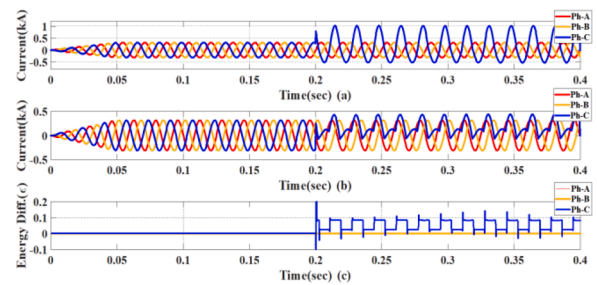


Fig. 24. HIF-LG (CG) Fault under GCRM, (a) Retrieved current signal at Bus-30 end, (b) Retrieved current signal at Bus-31 end, (c) EDS. .

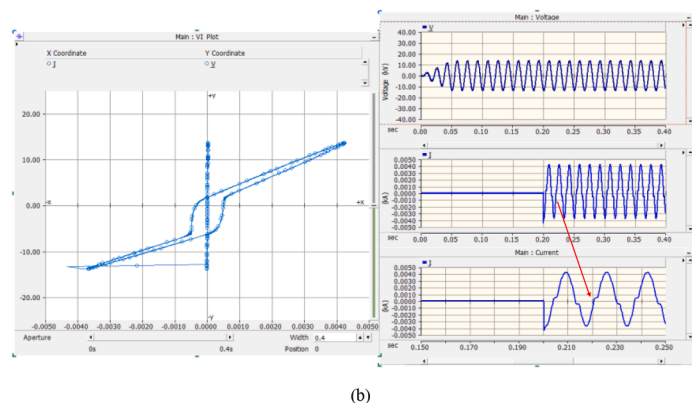
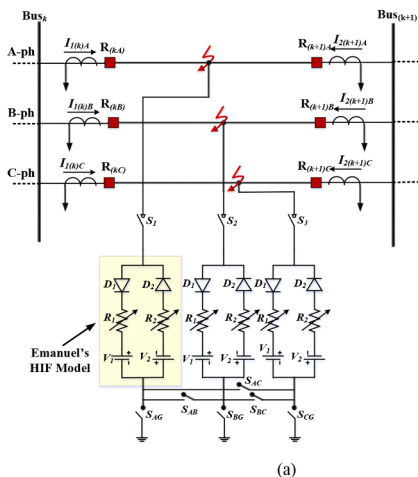


Fig. 23. HIF (a) Test model for HIF (b) Voltage-current characteristics curve (V₁ =8.7 kV, V₂ =11.3 kV, R₁ =1.2 kΩ, R₂=1.35 kΩ).

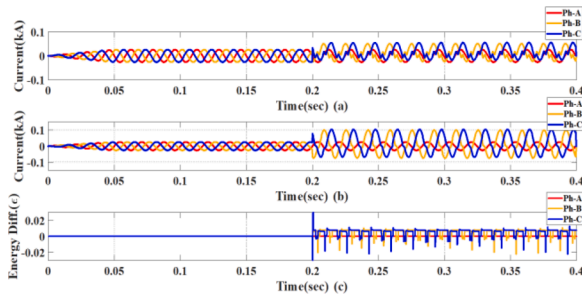


Fig. 25. HIF-LLG (BCG) Fault under AMRM, (a) Retrieved current signal at Bus-30 end, (b) Retrieved current signal at Bus-31 end, (c) EDS.

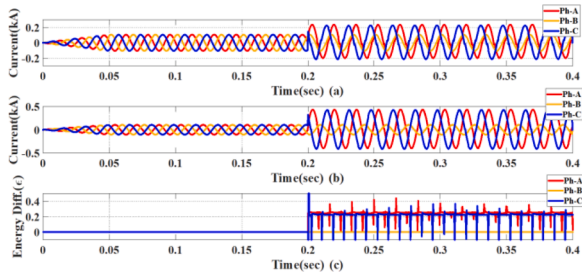


Fig. 26. HIF-LLG (ACG) Fault under AMRM, (a) Retrieved current signal at Bus-30 end, (b) Retrieved current signal at Bus-31 end, (c) EDS.

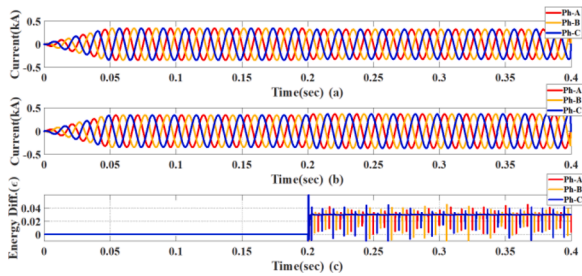


Fig. 27. HIF-LLL (ABC) Fault under GCLM, (a) Retrieved current signal at Bus-30 end, (b) Retrieved current signal at Bus-31 end, (c) EDS.

Table 5
Parameters of HIF model.

	Parameter		
Fault	LG	LLG	LLL
V ₁ (kV)	8.7–9	8.7–9	8.7–9
V ₂ (kV)	11.3–11.7	11.3–11.7	11.3–11.7
R ₁ (kΩ)	1.2–1.35	1.2–1.3	1.42–1.49
R ₂ (kΩ)	1.37–1.45	1.35–1.48	1.5–1.62

magnitude, also due to the fact that when a grounded HIF occurs near the zero-crossing point, the zero-sequence current waveform is distorted. However, EDSs are generated exactly at the inception of fault, and persists for entire duration of the fault, allowing detection of the fault exactly when it has occurred.

5.2.3. Load connection and disconnection

To realize the accuracy of proposed scheme, the event of sudden load connection and disconnection have been performed in Bus-26 and Bus-27 that can be considered from Fig. 1. The microgrid was configured as GCRM and the system loads are L-26 and L-27 each of (200 KW, 50 KVAR) connected initially to the respective buses (Bus-26, Bus-27). Operating current being 0.567 kA. At 0.15 s, both the loads are

Table 6
Operation of different HIFs.

Switch	Fault						
	LG	LLG	LLL	ACG	BCG	ABCG	ABC
S ₁	1	0	0	1	0	1	1
S ₂	0	1	0	1	1	0	1
S ₃	0	0	1	0	1	1	1
S _{AG}	1	0	0	1	0	1	1
S _{BG}	0	1	0	1	1	0	1
S _{CG}	0	0	1	0	1	1	1
S _{AB}	0	0	0	1	0	0	0
S _{BC}	0	0	0	0	1	0	0
S _{AC}	0	0	0	0	0	1	0

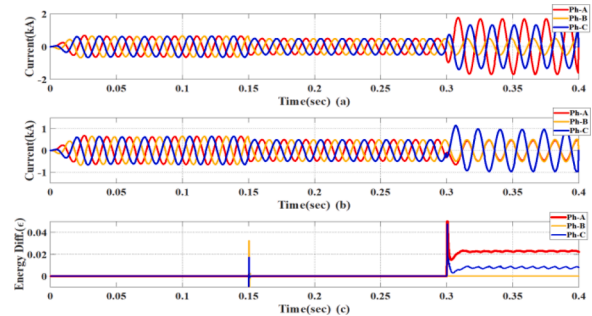


Fig. 28. Load disconnected and LL (AC) Fault under GCRM, (a) Retrieved current signal at Bus-26 end, (b) Retrieved current signal at Bus-27 end, (c) EDS.

suddenly disconnected from the buses, resulting in the decrease in current magnitude to be 0.475 kA. Then LL(AC) fault is initiated at 0.3 s as shown in Fig. 28. EDS conceives little humps at 0.15 s, however it is not sustained even though the loads are disconnected permanently from the buses. Here, the results are so promising which shows how the load disconnection event is effectively distinguishable from the fault. In order to verify the potency of the method, load connection event is also depicted in Fig. 29. Here also the microgrid was configured as GCRM and the system loads are L-26 and L-27 each of (200 KW, 50 KVAR) connected initially to the respective buses (Bus-26, Bus-27), operating current being 0.56 kA. A load (0.25 MW, 0.05 MVAR) is suddenly connected to Bus-27 along with the existing load L-27 at 0.15 s. The current increases to 0.67 kA. Here to distinguish the fault event with load changing operation, a unsymmetrical LL(AC) fault is also initiated at 0.3 s. Here from the result depicted in Fig. 29, it is evident that a very small hump is generated at 0.15 s for all three phases in the EDS, when the load changing operation is executed, however it has not sustained and when the ‘AC’ fault has taken place, the EDS sustained for pH-A and pH-C, while EDS for pH-B is zero. This substantially distinguishes any disturbances from system faults.

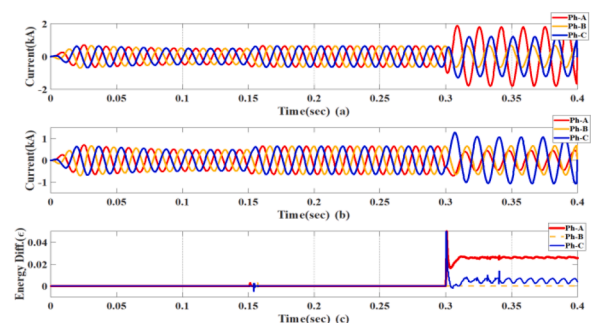


Fig. 29. Load connected and LL (AC) Fault under GCRM, (a) Retrieved current signal at Bus-26 end, (b) Retrieved current signal at Bus-27 end, (c) EDS.

5.2.4. DG connection and disconnection(outage)

Sudden connection and disconnection of DG is performed through hydro synchronous generator at Bus-11, which can be seen from Fig. 1. Microgrid has been configured as GCLM having the current level 0.645 kA prior to the disconnection of DG. At 0.15 s, DG has been disconnected and hereafter remain disconnected, meanwhile a LL (AC) fault is incepted at 0.3 s in the line connecting Bus-10 and 11. The current level substantially reduced to 0.45 kA due to disconnection of DG. The three phase current signals are shown in Fig. 30(a),(b). From Fig. 30(c), it can be observed that at 0.15th second very small humps have been produced for all three phases in the EDS, which has not been sustained. However, when the fault has encountered at 0.3 s, EDS for pH-A and pH-C initiates a spike at 0.3 s and sustained throughout the duration of the fault, while the EDS for pH-B remain zero. This can further be accentuated by performing the event of DG connection at Bus-11 at 0.15 s. In this case also, LL(AC) fault is initiated at 0.3 s, and the results can be seen from Fig. 31. Therefore, it can be realized that EDS based fault detection using TKEO can effectively distinguish the other system perturbations from system fault events.

5.2.5. Close-in fault identification

In order to identify the close-in fault, the current signals are retrieved from two ends of the bus and also from the one end of the adjacent bus, as shown in Fig. 32. Considering the estimated TKE for current signal $I_{1(k)p}[n]$ at kth bus end (at R_k) is $\Psi_{1(k)p \in A,B,C}$, estimated TKE for current signal $I_{2(k+1)p}[n]$ at $(k+1)$ th bus end (at R_{k+1}) is $\Psi_{2(k+1)p \in A,B,C}$, and for the adjacent bus $(k+2)$ (at R_{k+2}), the estimated TKE for current signal $I_{3(k+2)p}[n]$ is $\Psi_{3(k+2)p \in A,B,C}$. Here to detect the close-in fault, TKE difference of kth bus end current is compared with $(k+1)$ th bus end and $(k+2)$ th bus end currents. The outcome of the investigation is given in Table 7. If the TKE difference between the current measured at R_k and R_{k+2} is greater than zero, and if the TKE difference between the current measured at R_k and R_{k+1} is zero; the fault has occurred at point F_2 , which is essentially a strong sign for the occurrence of a close-in fault (Case:2, Table 7). If the TKE difference between the current measured at R_k and R_{k+1} is greater than zero and also if the TKE difference between the current measured at R_k and R_{k+2} is greater than zero; then it is an indication of line fault at point F_1 , which is at the middle of the line (Case:1, Table 7). Zero energy difference is a sharp indication of no fault condition.

To perform this aforementioned close-in fault detection algorithm, the lines connecting Bus-8,9 and 10 have been considered. The fault (F_1), which is considered at middle of the line is placed at 2.5 km from Bus-8 and 9, whereas the close-in fault (F_2) is considered at 10% of the line, i.e. at 0.5 km from the Bus-9, in the line connecting Bus-9 and 10. Fig. 32 has generalized the concept illustrated in this section which is a sub figure of the tested microgrid system shown in Fig. 1, therefore one can replace Bus_k as Bus-8, Bus_{k+1} as Bus-9 and Bus_{k+2} as Bus-10. The results shown in Figs. 33, 34 are obtained from the test case shown in Fig. 1, where the microgrid operation is performed under GCRM

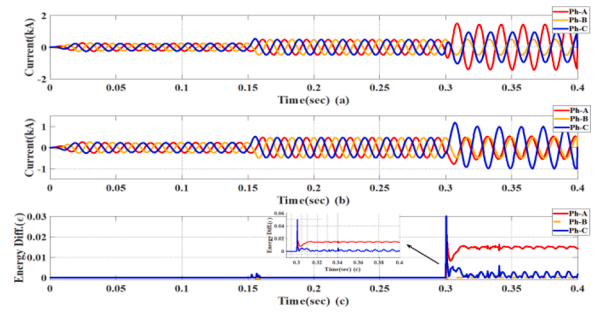


Fig. 31. DG connected and LL (AC) Fault under GCLM, (a) Retrieved current signal at Bus-26 end, (b) Retrieved current signal at Bus-27 end, (c) EDS.

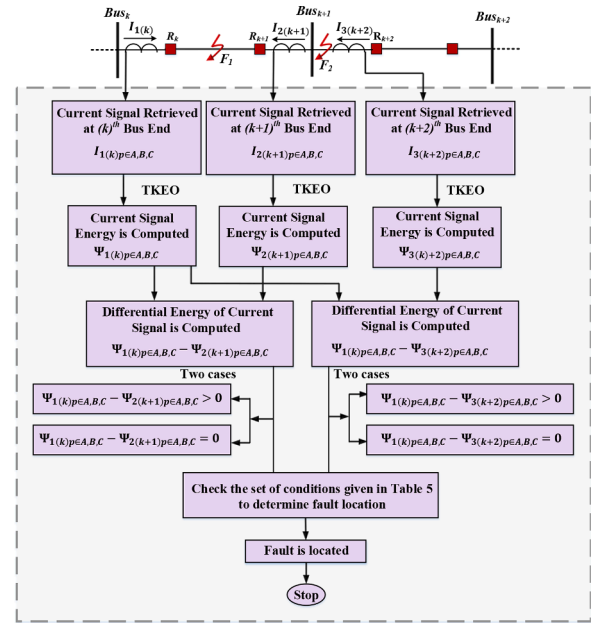


Fig. 32. Proposed fault location algorithm.

Table 7 Close-in fault identification criteria.

Events	Energy difference signals (EDSs)	Fault Location
Case:1	When $\Psi_{1(k)p \in A,B,C} - \Psi_{2(k+1)p \in A,B,C} > 0$; & $\Psi_{1(k)p \in A,B,C} - \Psi_{3(k+2)p \in A,B,C} > 0$	Line fault at point F_1
Case:2	When $\Psi_{1(k)p \in A,B,C} - \Psi_{2(k+1)p \in A,B,C} = 0$; & $\Psi_{1(k)p \in A,B,C} - \Psi_{3(k+2)p \in A,B,C} > 0$	Close-in fault at point F_2
Case:3	When $\Psi_{1(k)p \in A,B,C} - \Psi_{2(k+1)p \in A,B,C} = 0$; & $\Psi_{1(k)p \in A,B,C} - \Psi_{3(k+2)p \in A,B,C} = 0$	No fault

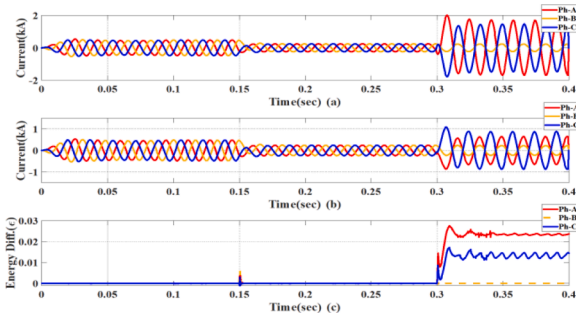


Fig. 30. DG disconnected and LL (AC) Fault under GCLM, (a) Retrieved current signal at Bus-26 end, (b) Retrieved current signal at Bus-27 end, (c)EDS.

configuration with LG (BG) fault having R_f of 0.01 Ω , and FIA of 0° . Fig. 33 shows the result for LG (BG) fault under GCRM at F_1 . It satisfies the condition mentioned in Case-1, given in Table 7. Fig. 33(a), (b), (c) show the retrieved current signal at Bus-8 end, Bus-9 end, and Bus-9 end from adjacent line. Here, Fig. 33(d) illustrates the EDS obtained from Bus-8 end measured current and Bus-9 end of the same line, while Fig. 33(e) shows the EDS of Bus-8 end measured current and Bus-9 end of the adjacent line. The LG (BG) fault has occurred at 0.3 s. thus, both the EDSs produce sharp spike at 0.3 s, consolidating the event of middle line fault at the line connecting Bus-8, 9. On the other hand, Fig. 34 shows the result for case-2 of Table 7. In Fig. 34(d), it can be observed that the EDS of Bus-8 end measured current and Bus-9 end measured current of the same line is zero due to the close-in fault in the adjacent line at F_2 (shown in Fig. 32). Whereas, in Fig. 34(e), the EDS of Bus-8 end

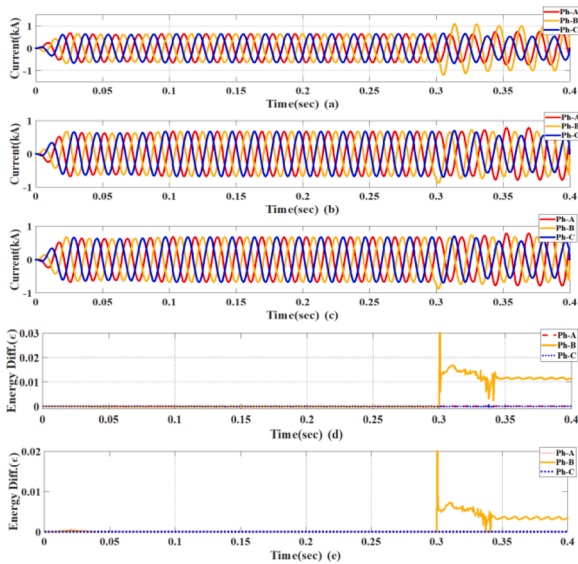


Fig. 33. LG (BG) Fault under GCRM at F_1 (Fig. 20), (a) Retrieved current signal at Bus-8 end, (b) Retrieved current signal at Bus-9 end, (c) Retrieved current signal at Bus-9 from adjacent line, (d) EDS of Bus-8 end measured current and Bus-9 end of the same line, (e) EDS of Bus-8 end measured current and Bus-9 end of the adjacent line.

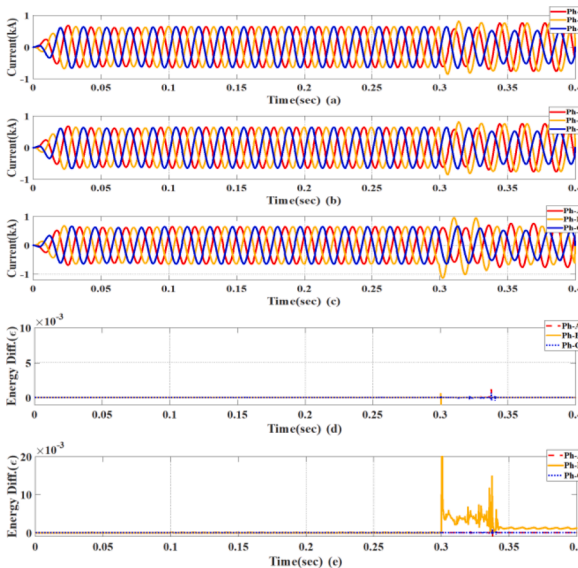


Fig. 34. LG (BG) Fault under GCRM at F_2 (Fig. 20), (a) Retrieved current signal at Bus-8 end, (b) Retrieved current signal at Bus-9 end, (c) Retrieved current signal at Bus-8 from adjacent line, (d) EDS of Bus-8 end measured current and Bus-9 end of the same line, (e) EDS of Bus-8 end measured current and Bus-9 end of the adjacent line.

measured current and Bus-9 end of the adjacent line is showing large spike at 0.3 s exactly during the fault inception and it sustained during the entire duration of the fault. This essentially indicates the close-in fault, which is created at 10% of the line connecting the buses 9 and 10.

5.2.6. Effect of DG intermittency in fault detection

The intermittent nature of DG, precisely the varying irradiation and temperature of solar system and variable wind speed, decisively affects the power generation output of PV based DG and wind energy based DGs. This intermittency results in power swing, leading to introduce dynamic voltage and current. In order to study the DG intermittency,

solar irradiation and temperature is varied from 800 to 1200 W/m² and 25 °C-40 °C, respectively. Whereas the wind speed is varied from 7 to 15 m/s. As the PV is connected to bus-27, the fault study is performed in the line connecting Bus-26, 27, operating under GCRM operation. The study for wind power intermittency is performed in the line connecting Bus-32, 33, operating under GCRM configuration. From Figs. 35, 36, it can be seen that the currents are behaving dynamically. Here two fault cases have been simulated in order to realize the selectivity of the proposed scheme. One fault case is studied at higher current level, and another at lower current level. First fault is a LG(AG) created at 0.3 s and it is removed at 0.39 s, whereas the second fault is a LL(BC) fault simulated at 0.6 s and removed at 0.69 s. It is evident that the EDS for phase-A surges exactly when the fault has taken place in the system and extinguishes exactly when the fault is removed. The EDS for other two phases remain zero until the second fault case is studied at 0.6 s, where due to LL(BC) fault, the EDS surges and persists till the duration of the fault, i.e. 0.09 s. In this time, phase-A EDS value retains zero. This result infers the excellent selectivity of this approach, while detecting the fault under dynamic current situation.

5.2.7. Fault detection under heavy loading condition

Heavy load variation in a shorter period of time may cause sudden temporary overloading to some part of the microgrid, and creates ambiguity for the protection devices. In order to examine the overloading event and to study its effect on fault detection, different cases are considered where the fault is simulated in the distribution line connecting bus-8,9 (can be seen from Fig. 1).

i Case 1: The microgrid was configured initially as AMLM, and normal system loads L-8 and L-9 each of (200 KW, 50 KVAR) were connected to the respective buses (Bus-8, Bus-9). At 0.001 s, a heavy three-phase load of 15 MW, 3 MVAR is connected at bus-8, and disconnected at 0.01 s which creates initial inrush current for all three phases as shown in Fig. 37. This instantaneous load connection, and disconnection is performed to realize the temporary overloading condition. Secondly, the load (15 MW, 3 MVAR) is further connected at 0.2 s, and remain connected, which creates the heavy loading condition. In such a situation LG(AG) fault is encountered at 0.3 s, for the duration of 0.09 s. The generated EDS can be seen in Fig. 37(c). EDS conceives humps at 0.001 s, when temporary overloading is occurring and also at 0.2 s, when the heavy three-phase loading has happened. However, when the fault is taking place at 0.3 s the generated EDS of the faulted phase-A is sustained for 0.09 s till the duration of the fault, whereas for non-faulted phase EDS retain zero value. In order to show the selectivity of the scheme, the fault is removed after 0.09 s, and exactly then the EDS again goes zero. Here the obtained results are so convincing which shows excellent

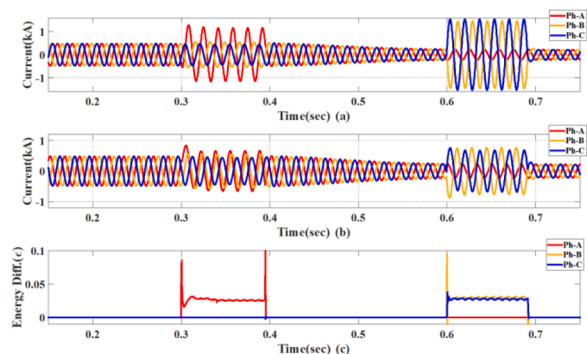


Fig. 35. LG (AG) & LL(BC) Faults under GCRM at the middle of the line connecting Bus-26, 27, (solar irradiation is varying from 800 to 1200 W/m², and temperature is varying from 25°C-40°C), (a) Retrieved current signal at Bus-26 end, (b) Retrieved current signal at Bus-27 end, (c) EDS.

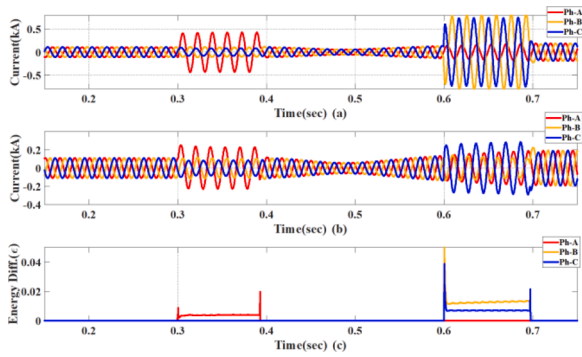


Fig. 36. LG (AG) & LL(BC) Faults under GCRM at the middle of the line connecting Bus-32, 33, (wind speed is varying from 7 to 15 m/s), (a) Retrieved current signal at Bus-32 end, (b) Retrieved current signal at Bus-33 end, (c) EDS. .

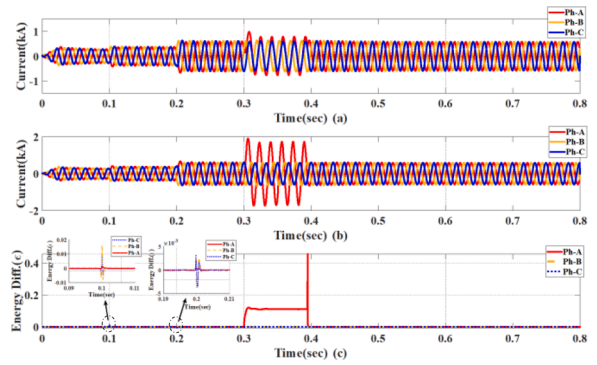


Fig. 39. LG (AG) Fault at line connecting Bus-8,9, under successive heavy loading condition AMLM, (a) Retrieved current signal at Bus-8 end, (b) Retrieved current signal at Bus-9 end, (c) EDS.

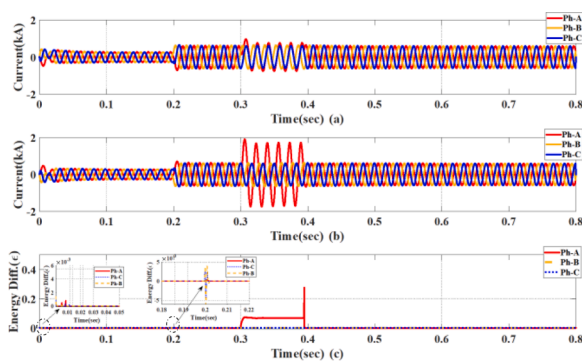


Fig. 37. LG (AG) Fault at line connecting Bus-8,9 under temporary overloading condition at starting in AMLM, (a) Retrieved current signal at Bus-8 end, (b) Retrieved current signal at Bus-9 end, (c) EDS. .

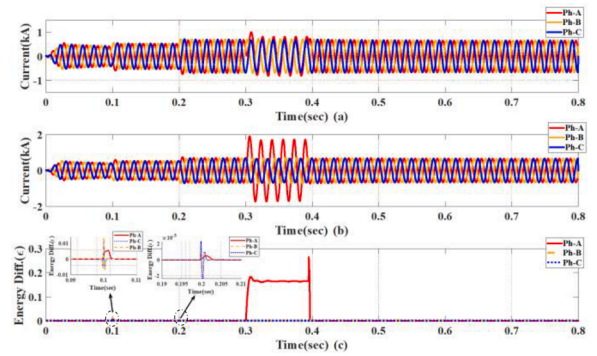


Fig. 40. LG (AG) Fault at line connecting Bus-8,9, under successive heavy loading condition GCLM, (a) Retrieved current signal at Bus-8 end, (b) Retrieved current signal at Bus-9 end, (c) EDS.

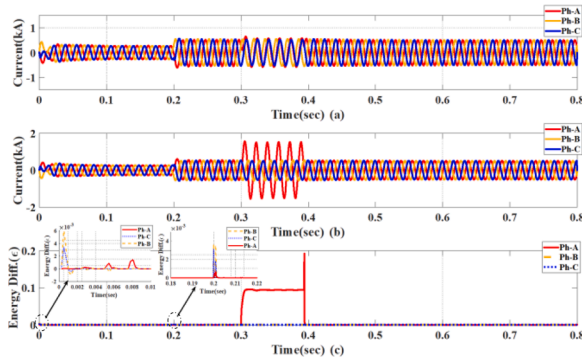


Fig. 38. LG (AG) Fault at line connecting Bus-8,9, under temporary overloading condition at starting GCLM, (a) Retrieved current signal at Bus-8 end, (b) Retrieved current signal at Bus-9 end, (c) EDS. .

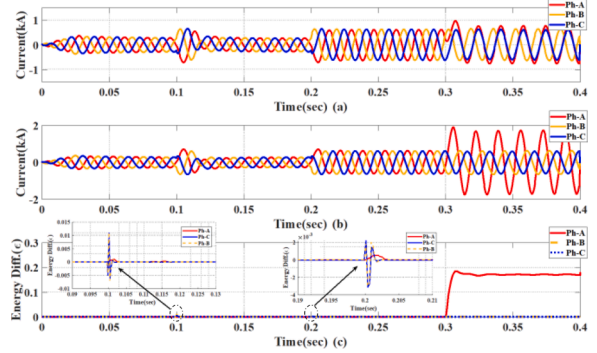


Fig. 41. LG (AG) Fault at line connecting Bus-8,9, under temporary overloading condition at 0.1 s AMLM, (a) Retrieved current signal at Bus-8 end, (b) Retrieved current signal at Bus-9 end, (c) EDS. .

selectivity and distinguishing capability between fault and two different loading events. Fig. 38. shows the result for GCLM configured operation.

- ii Case 2: Another test bed is prepared, where, two-step successive loading is performed. Here 15 MW, 3 MVAR load is connected at 0.1 s and 10 MW, 2 MVAR load is further connected at 0.2 s and the LG (AG) fault has encountered at 0.3 s with a duration of 0.09 s in the total 25 MW, 5 MVAR loaded heavily distribution line. The results of successive loading phenomena for AMLM and GCLM are shown in Figs. 39, 40 respectively.

- iii Case 3: Another case study is performed, where the temporary overloading time is increased from the first case study. Here, the overloading phenomena is considered to be occurring for the duration of 0.01 s, that can be seen from Fig. 41. 15 MW, 3 MVAR load is connected to the system at 0.1 s and load is cut off at 0.11 s. Further the load is connected at 0.2 s and LG(AG) fault has encountered at 0.3 s as given in Fig. 41. This test bed is selected in order to show the temporary overloading, and fault detection under heavy loaded microgrid in the same frame. From the result, it can be realised that, when the loads are connected, the EDS generates gentle humps, and it does not persist, but when fault occurs under this heavily loaded condition, EDS sustained. However, this can be observed that, the

hump generated for temporary overloading event is more sharper than the instant heavy loading event and the proposed technique can seamlessly distinguish the loading phenomenon from actual system faults.

6. Discussion

The objective of this work is to provide a simple and well-efficient fault detection scheme for the DG integrated microgrid system which can work proficiently for any microgrid structure operating under various operating modes. The sustaining non-zero value of the energy difference index triggers the fault detection algorithm. For obtaining the EDS using TKEO, sliding window is used in order to capture the TKE data for each sample. The current data is sampled at a sampling frequency of 3.84 kHz as mentioned before; therefore, the window width is so selected that can capture enough information for executing the proposed algorithm. While providing a finer time resolution a wider window may contain redundant data, whereas a narrow window may suffer from less information. Bearing that in mind, a 2.083 ms window is chosen that can capture 8 samples/window containing enough information regarding the TKE. It can be seen in Fig. 42(c) and 43(c), which are the Zoomed version of Figs. 10(c) and 11(c), respectively. This proposed technique is faster than any communication assisted AOCB scheme, as it can be observed that the fault is detected within 2–2.5 ms, which is well under the permissible limit of microgrid fault detection time. Moreover, this technique requires only three consecutive sample data and three mathematical operations (two multiplications, one subtraction per sample) to execute the TKEO algorithm, thus it does not suffer from heavy computational burden unlike the optimization-based techniques have [11]. As one can see that the nonlinear formulation and heavy computation is a tedious process that essentially increase the fault detection time. Fig. 43

Those techniques use extensive frequency domain analysis of signal followed by artificial intelligence techniques also suffers from large detection time due to successive processing of signal [23]. In [23], the fault detection time is observed to be 1.5–2.5 cycles (60 Hz system); i.e. 25–41.66 ms, which is much slower than that of this proposed scheme. Moreover, the need of computation of finer scaling and also the threshold setting for different fault cases potentially increase the operational complexity. Nonetheless, most of the proposed techniques have not considered different microgrid topologies (GCRM, GCLM, AMRM, AMLM) in same work. Therefore, those methods have not been tested for all possible fault levels, which is vigorously studied in this work with all possible fault types with varying fault resistance and FIA. Moreover, it is worth noting that most severe events of HIF can also be detected along with LRF by the same proposed algorithm.

Further, while exploring the consolidated benefits of the proposed

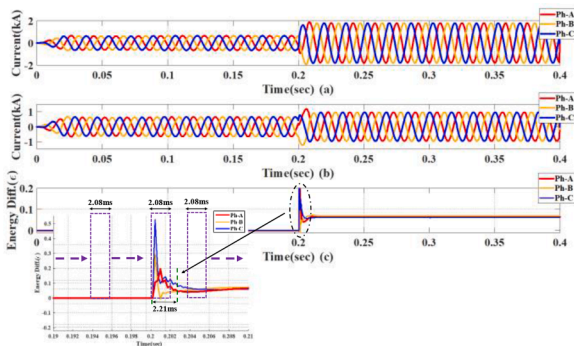


Fig. 42. LLLG (ABCG) Fault under GCLM, at middle of the line (2.5 km from both buses) connecting Bus-8,9, FIA=0°, R_f=0.01 Ω, (a) Retrieved current signal at Bus-8 end, (b) Retrieved current signal at Bus-9 end, (c) Captured EDS with sliding window.

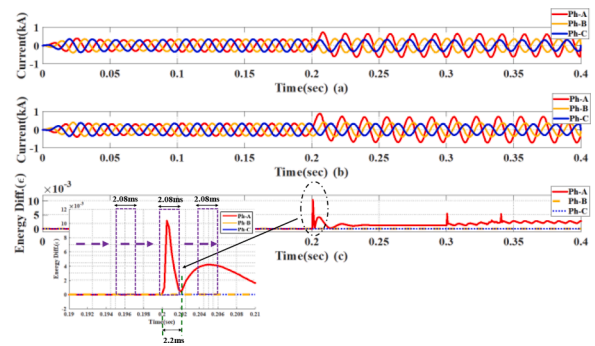


Fig. 43. LG (AG) Fault under AMRM, at middle of the line (2.5 km from both buses) connecting Bus-8,9, FIA=0°, R_f=0.01 Ω, (a) Retrieved current signal at Bus-8 end, (b) Retrieved current signal at Bus-9 end, (c) Captured EDS with sliding window.

scheme, it can be seen that this scheme does not require communication between relays in order to trigger the protection unit. Therefore, in one way, it is cost-effective as the cost associated with advance communication is removed, and in another way the chance of catastrophic collapse due to communication failure is essentially eliminated.

This article has essentially emphasized on the following aspects in order to provide its broader applicability:

- ü It has shown effective results for four different operations of the microgrid in grid connected and autonomous mode with different fault resistances and varying FIA.
- ü HIF modelling and simulation results are described, and it is shown that the proposed scheme is capable to detect the severe HIF at different microgrid operation states.
- ü It has shown convincing results, while distinguishing the other power system disturbances, such as DG outage, load switching from fault events.
- ü Performance of the proposed protection technique is also validated for heavy loading conditions.
- ü The effectiveness of the proposed scheme is also examined in power swing conditions, which is realized by considering the effect of DG intermittency (by varying irradiance on solar panels and variable wind speed).

The comparative summary with other existing microgrid protection approaches with this proposed technique has been evaluated by accounting the main features, mentioned in Table 8 and the performance indices matrix is given in Table 9. It can be seen from the performance indices matrix that the system disturbance detection accuracy has reached up to 99%, which is confronting the excellent efficacy of the proposed scheme, depicted in Fig. 44.

7. Conclusion

This article aims to propose a simple cost-effective protection approach that can resolve the protection issues associated with DG integrated emerging microgrid. It can be inferred that the proposed TKEO based scheme, works effectively under different topologies and mode of microgrid operations. Also, it can effectively detect all types of unsymmetrical, symmetrical faults under varying fault resistance and FIA, along with most severe HIFs. Moreover, it can effectively distinguish the non-fault events from system faults with a high detection accuracy around 98–99%. The distinctiveness of this technique is that, by using the single mathematical computation tool in time domain, fault detection and fault type classification can be done so effectively. This technique is capable to detect the fault within 2–2.5 ms, which has substantially reduced the fault detection time by approximately 10% from most of the existing methods. Nonetheless, this technique is

Table 8
Comparison with existing microgrid protection techniques.

Protection Schemes [Ref.]	Comparison Aspects	Mode of operation		MG topology		DG type		Fault type		Selectivity & Reliability	Communi- cation	Cost
		GCMO	AMO	Radial	Loop	RMDG	IIDG	LRF	HIF			
AOCP [9–11].												
[9]		✓	✓	✓	–	✓	–	✓	–	⦿	✓	▲
[10]		✓	✓	✓	–	✓	–	✓	–	⦿	✓	▲
[11]		✓	✓	–	✓	✓	–	✓	–	⦿	✓	▲
Differential protection [36]		–	✓	✓	–	✓	–	✓	–	⦿	✓	▲
Distance protection [37]		✓	–	✓	–	✓	–	✓	–	⦿	–	⦿
Voltage based [38]		–	✓	✓	–	–	✓	✓	–	⦿	–	⦿
Time-frequency transform [24, 25].												
[24]		✓	–	✓	–	–	✓	✓	–	⦿	–	⦿
[25]		✓	–	✓	–	–	–	✓	–	⦿	✓	▲
WAMPS using PMU [18]		✓	✓	–	✓	✓	✓	✓	–	⦿	✓	▲
Hybrid protection techniques including neural network, machine learning, etc. [39, 40]												
[39]		✓	–	–	✓	✓	–	✓	–	⦿	✓	▲
[40]		✓	–	–	✓	✓	–	✓	–	⦿	–	⦿
Proposed Scheme		✓	✓	✓	✓	✓	✓	✓	✓	▲	–	⦿

Symbol indication: Low: ‘⦿’, Moderate: ‘⦿’, High: ‘▲’.

Table 9
Performance Indices matrix of the test cases.

Events	Total no. of test case(App.)	Microgrid configuration				Correct detection	Wrong detection	% Accuracy of detection
		GCRM	GCLM	AMRM	AMLM			
✓ No fault	400	100	100	100	100	398	2	99.5
✓ Fault	1536	384	384	384	384	1528	8	99.34
✓ Load switching	960	240	240	240	240	952	8	99.16
✓ DG outage	600	150	150	150	150	594	6	99.00
✓ Temporary overloading	780	195	195	195	195	767	13	98.33
✓ DG intermittency	840	210	210	210	210	834	6	99.28
✓ Close-in fault	560	140	140	140	140	553	7	98.75
✓ HIF	800	200	200	200	200	785	15	98.125

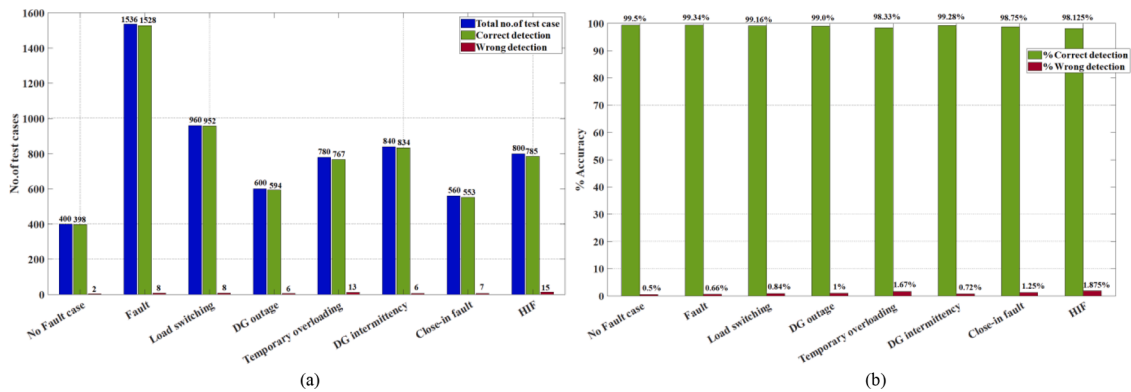


Fig. 44. Performance accuracy plot for different case studies, (a) Actual measured values, (b) Accuracy measured in%.

capable to reduce the computing overheads that are associated with complex optimization based AOCF techniques, and detail frequency domain analysis based methods. As this technique is essentially reckoning on the energy difference of current signals, it does not suffer from the difficulties confronted with dynamic current behaviour of a microgrid. Therefore, the ability of anticipating the system faults accurately has preserved the effectiveness of the suggested protection strategy. This method is so established that it can proficiently work in any microgrid structure, therefore proposed scheme has good scope for its broad applicability.

CRedit authorship contribution statement

Ankan Chandra: Conceptualization, Methodology, Software, Validation, Writing – original draft. **G.K. Singh:** Validation, Visualization, Investigation, Writing – review & editing, Supervision. **Vinay Pant:**

Visualization, Investigation, Supervision, Writing – review & editing.

Declaration of Competing Interest

The authors declare that they have no known competing financial interests or personal relationships that could have appeared to influence the work reported in this paper.

Data Availability

No data was used for the research described in the article.

References

- [1] S.A. Arefifar, Y.A.R.I. Mohamed, T.H.M. El-Fouly, Optimum microgrid design for enhancing reliability and supply-security, *IEEE Trans. Smart Grid*. 4 (2013) 1567–1575, <https://doi.org/10.1109/TSG.2013.2259854>.
- [2] M. Shahidehpour, J.F. Clair, A functional microgrid for enhancing reliability, sustainability, and energy efficiency, *Electr. J.* 25 (2012) 21–28, <https://doi.org/10.1016/j.tej.2012.09.015>.
- [3] A. Chandra, G.K. Singh, V. Pant, Protection of AC microgrid integrated with renewable energy sources – a research review and future trends, *Electr. Power Syst. Res.* 193 (2021), 107036, <https://doi.org/10.1016/j.epsr.2021.107036>.
- [4] A. Chandra, G.K. Singh, V. Pant, Protection techniques for DC microgrid- a review, *Electr. Power Syst. Res.* 187 (2020), 106439, <https://doi.org/10.1016/j.epsr.2020.106439>.
- [5] S.C. Vegunta, M.J. Higginson, Y.E. Kenarangui, G.T. Li, D.W. Zabel, M. Tasdighi, A. Shadman, AC microgrid protection system design challenges—a practical experience, *Energies* 14 (2021) 1–23, <https://doi.org/10.3390/en14072016>.
- [6] N. Nimpitiwan, G.T. Heydt, R. Ayyanar, S. Suryanarayanan, Fault current contribution from synchronous machine and inverter based distributed generators, *IEEE Trans. Power Deliv.* 22 (2007) 634–641, <https://doi.org/10.1109/TPWRD.2006.881440>.
- [7] K.I. Jennett, C.D. Booth, F. Coffele, A.J. Roscoe, Investigation of the sympathetic tripping problem in power systems with large penetrations of distributed generation, *IET Gener. Transm. Distrib.* 9 (2015) 379–385, <https://doi.org/10.1049/iet-gtd.2014.0169>.
- [8] F. Coffele, C. Booth, A. Dyško, G. Burt, Quantitative analysis of network protection blinding for systems incorporating distributed generation, *IET Gener. Transm. Distrib.* 6 (2012) 1218–1224, <https://doi.org/10.1049/iet-gtd.2012.0381>.
- [9] P. Mahat, Z. Chen, B. Bak-Jensen, C.L. Bak, A simple adaptive overcurrent protection of distribution systems with distributed generation, *IEEE Trans. Smart Grid*. 2 (2011) 428–437, <https://doi.org/10.1109/TSG.2011.2149550>.
- [10] H. Muda, P. Jena, Superimposed adaptive sequence current based microgrid protection: a new technique, *IEEE Trans. Power Deliv.* 32 (2017) 757–767, <https://doi.org/10.1109/TPWRD.2016.2601921>.
- [11] H.M. Sharaf, H.H. Zeineldin, E. El-Saadany, Protection coordination for microgrids with grid-connected and islanded capabilities using communication assisted dual setting directional overcurrent relays, *IEEE Trans. Smart Grid*. 9 (2018) 143–151, <https://doi.org/10.1109/TSG.2016.2546961>.
- [12] M.M. Mansour, S.F. Mekhamer, N.E.S. El-Kharbawe, A modified particle swarm optimizer for the coordination of directional overcurrent relays, *IEEE Trans. Power Deliv.* 22 (2007) 1400–1410, <https://doi.org/10.1109/TPWRD.2007.899259>.
- [13] J. Moirangthem, K.R. Krishnanand, S.S. Dash, R. Ramaswami, Adaptive differential evolution algorithm for solving non-linear coordination problem of directional overcurrent relays, *IET Gener. Transm. Distrib.* 7 (2013) 329–336, <https://doi.org/10.1049/iet-gtd.2012.0110>.
- [14] A. Hussain, H.M. Kim, A hybrid framework for adaptive protection of microgrids based on IEC 61850, *Int. J. Smart Home*. 10 (2016) 285–296, <https://doi.org/10.14257/ijsh.2016.10.5.26>.
- [15] H. Laaksonen, D. Ishchenko, A. Oudalov, Adaptive protection and microgrid control design for Hailuoto Island, *IEEE Trans. Smart Grid*. 5 (2014) 1486–1493, <https://doi.org/10.1109/TSG.2013.2287672>.
- [16] H. Wan, K.K. Li, K.P. Wong, An adaptive multiagent approach to protection relay coordination with distributed generators in industrial power distribution system, *IEEE Trans. Ind. Appl.* 46 (2010) 2118–2124, <https://doi.org/10.1109/TIA.2010.2059492>.
- [17] V. Terzija, G. Valverde, D. Cai, P. Regulski, V. Madani, J. Fitch, S. Skok, M. M. Begovic, A. Phadke, Wide-area monitoring, protection, and control of future electric power networks, *Proc. IEEE*. 99 (2011) 80–93, <https://doi.org/10.1109/JPROC.2010.2060450>.
- [18] N.K. Sharma, S.R. Samantaray, Assessment of PMU-based wide-area angle criterion for fault detection in microgrid, *IET Gener. Transm. Distrib.* 13 (2019) 4301–4310, <https://doi.org/10.1049/iet-gtd.2019.0027>.
- [19] A. Carta, N. Locci, C. Muscas, S. Sulis, A flexible GPS-based system for synchronized phasor measurement in electric distribution networks, *IEEE Trans. Instrum. Meas.* 57 (2008) 2450–2456, <https://doi.org/10.1109/TIM.2008.924930>.
- [20] H.R. Baghaee, D. Mlakic, S. Nikolovski, T. Dragicevic, Anti-islanding protection of PV-based microgrids consisting of PHEVs using SVMs, *IEEE Trans. Smart Grid*. 11 (2020) 483–500, <https://doi.org/10.1109/TSG.2019.2924290>.
- [21] W.H. Kim, J.Y. Kim, W.K. Chae, G. Kim, C.K. Lee, LSTM-based fault direction estimation and protection coordination for networked distribution system, *IEEE Access* 10 (2022) 40348–40357, <https://doi.org/10.1109/ACCESS.2022.3166836>.
- [22] E. Casagrande, W.L. Woon, H.H. Zeineldin, N.H. Kan'an, Data mining approach to fault detection for isolated inverter-based microgrids, *IET Gener. Transm. Distrib.* 7 (2013) 745–754, <https://doi.org/10.1049/iet-gtd.2012.0518>.
- [23] D.P. Mishra, S.R. Samantaray, G. Joos, A combined wavelet and data-mining based intelligent protection scheme for microgrid, *IEEE Trans. Smart Grid*. 7 (2016) 2295–2304, <https://doi.org/10.1109/TSG.2015.2487501>.
- [24] S. Netsanet, J. Zhang, D. Zheng, Bagged decision trees based scheme of microgrid protection using windowed fast fourier and wavelet transforms, *Electron* 7 (2018), <https://doi.org/10.3390/electronics7050061>.
- [25] S. AsghariGovar, S. Heidari, H. Seyedi, S. Ghazemzadeh, P. Pourghasem, Adaptive CWT-based overcurrent protection for smart distribution grids considering CT saturation and high-impedance fault, *IET Gener. Transm. Distrib.* 12 (2018) 1366–1373, <https://doi.org/10.1049/iet-gtd.2017.0887>.
- [26] M.J.B. Reddy, D.V. Rajesh, P. Gopakumar, D.K. Mohanta, Smart fault location for smart grid operation using RTUs and computational intelligence techniques, *IEEE Syst. J.* 8 (2014) 1260–1271, <https://doi.org/10.1109/JSYST.2014.2303833>.
- [27] N.E. Huang, Z. Shen, S.R. Long, M.C. Wu, H.H. Snin, Q. Zheng, N.C. Yen, C.C. Tung, H.H. Liu, The empirical mode decomposition and the Hilbert spectrum for nonlinear and non-stationary time series analysis, *Proc. R. Soc. A Math. Phys. Eng. Sci.* 454 (1998) 903–995, <https://doi.org/10.1098/rspa.1998.0193>.
- [28] J.F. Kaiser, On a simple algorithm to calculate the “energy” of a signal, *ICASSP, IEEE Int. Conf. Acoust. Speech Signal Process.* - Proc. 1 (1990) 381–384, <https://doi.org/10.1109/icassp.1990.115702>.
- [29] P. Maragos, J.F. Kaiser, T.F. Quatieri, Energy separation in signal modulations with application to speech analysis, *IEEE Transactions on Signal Processing* 41 (1993) 3024–3051.
- [30] Teager, H.M., & Teager, S.M. (1990). Evidence for Nonlinear Sound Production Mechanisms in the Vocal Tract. 241–261.
- [31] J. Kumar, P. Jena, Solution to fault detection during power swing using Teager-Kaiser energy operator, *Arab. J. Sci. Eng.* 42 (2017) 5003–5013, <https://doi.org/10.1007/s13369-017-2538-7>.
- [32] D.A. Kaiser, J.F. Kaiser, Estimation of power systems amplitudes, frequencies, and phase characteristics using Energy Operators, in: 2012 IEEE Energy Convers. Congr. Expo. ECCE 2012, 2012, pp. 930–937, <https://doi.org/10.1109/ECCE.2012.6342719>.
- [33] P. Henríquez Rodríguez, J.B. Alonso, M.A. Ferrer, C.M. Travieso, Application of the Teager-Kaiser energy operator in bearing fault diagnosis, *ISA Trans.* 52 (2013) 278–284, <https://doi.org/10.1016/j.isatra.2012.12.006>.
- [34] V. Torres, J.L. Guardado, H.F. Ruiz, S. Maximov, Modeling and detection of high impedance faults, *Int. J. Electr. Power Energy Syst.* 61 (2014) 163–172, <https://doi.org/10.1016/j.ijepes.2014.03.046>.
- [35] E.M.G.A.E. Emanuel, High impedance fault aecing on sandy soil in 15kV distribution feeders: contributions to the evaluation of the low frequency spectrum, *IEEE Trans. Power Deliv.* 5 (1990) 676–686.
- [36] K. Dubej, P. Jena, Impedance angle-based differential protection scheme for microgrid feeders, *IEEE Syst. J.* (2020) 1–10, <https://doi.org/10.1109/jsyst.2020.3005645>.
- [37] K. El-Aroudi, G. Joos, Performance of interconnection protection based on distance relaying for wind power distributed generation, *IEEE Trans. Power Deliv.* 33 (2018) 620–629, <https://doi.org/10.1109/TPWRD.2017.2693292>.
- [38] H. Al-Nasseri, M.A. Redfern, F. Li, A voltage based protection for micro-grids containing power electronic converters, in: 2006 IEEE Power Eng. Soc. Gen. Meet. PES., 2006, pp. 1–7, <https://doi.org/10.1109/pes.2006.1709423>.
- [39] H. Lin, K. Sun, Z.H. Tan, C. Liu, J.M. Guerrero, J.C. Vasquez, Adaptive protection combined with machine learning for microgrids, *IET Gener. Transm. Distrib.* 13 (2019) 770–779, <https://doi.org/10.1049/iet-gtd.2018.6230>.
- [40] S.B.A. Bukhari, C.H. Kim, K.K. Mehmood, R. Haider, M.S.U. Zaman, Convolutional neural network-based intelligent protection strategy for microgrids, *IET Gener. Transm. Distrib.* 14 (2020) 1177–1185, <https://doi.org/10.1049/iet-gtd.2018.7049>.